

ViTAL: Vision-Based Terrain-Aware Locomotion for Legged Robots

Shamel Fahmi^{ID}, Student Member, IEEE, Victor Barasuol, Domingo Esteban^{ID}, Octavio Villarreal^{ID}, and Claudio Semini^{ID}, Member, IEEE

Abstract—This article focuses on vision-based planning strategies for legged robots that separate locomotion planning into foothold selection and pose adaptation. Current pose adaptation strategies optimize the robot’s body pose relative to *given* footholds. If these footholds are not reached, the robot may end up in a state with no reachable safe footholds. Therefore, we present a vision-based terrain-aware locomotion (ViTAL) strategy that consists of novel pose adaptation and foothold selection algorithms. ViTAL introduces a different paradigm in pose adaptation that does not optimize the body pose relative to given footholds, but the body pose that maximizes the chances of the legs in reaching safe footholds. ViTAL plans footholds and poses based on skills that characterize the robot’s capabilities and its terrain awareness. We use the 90-kg HyQ and 140-kg HyQReal quadruped robots to validate ViTAL and show that they are able to climb various obstacles, including stairs, gaps, and rough terrains, at different speeds and gaits. We compare ViTAL with a baseline strategy that selects the robot pose based on given selected footholds and show that ViTAL outperforms the baseline.

Index Terms—Legged robots, optimization and optimal control, visual learning, whole-body motion planning and control.

NOMENCLATURE

\mathcal{F}	Set of safe footholds.
n_{sf}	Number of safe footholds.
CNN	Convolutional neural network.
FC	Foot trajectory collision.
FEC	Foothold evaluation criteria.
HyQ	Hydraulically actuated quadruped.
KF	Kinematic feasibility.
LC	Leg collision.
MPC	Model-predictive control.

Manuscript received 9 August 2022; revised 17 October 2022; accepted 7 November 2022. Date of publication 29 November 2022; date of current version 5 April 2023. This article was recommended for publication by Associate Editor J. Kober and Editor E. Yoshida upon evaluation of the reviewers’ comments. (*Corresponding author:* Shamel Fahmi.)

Shamel Fahmi was with the Dynamic Legged Systems Lab, Istituto Italiano di Tecnologia, 16163 Genoa, Italy. He is now with the Biomimetic Robotics Lab, Massachusetts Institute of Technology, Cambridge, MA 02139 USA (e-mail: sfahmi@mit.edu).

Victor Barasuol and Claudio Semini are with the Dynamic Legged Systems Lab, Istituto Italiano di Tecnologia, 16163 Genoa, Italy (e-mail: victor.barasuol@iit.it; claudio.semini@iit.it).

Domingo Esteban and Octavio Villarreal were with the Dynamic Legged Systems Lab, Istituto Italiano di Tecnologia, 16163 Genoa, Italy.

This article has supplementary material provided by the authors and color versions of one or more figures available at <https://doi.org/10.1109/TRO.2022.3222958>.

Digital Object Identifier 10.1109/TRO.2022.3222958

RCF	Reactive controller framework.
RL	Reinforcement learning.
TAL	Terrain-aware locomotion.
TBR	Terrain-based body reference.
TO	Trajectory optimization.
TR	Terrain roughness.
VFA	Vision-based foothold adaptation.
ViTAL	Vision-based terrain-aware locomotion.
VPA	Vision-based pose adaptation.
WBC	Whole-body controller.

I. INTRODUCTION

LEGGED robots have shown remarkable agile capabilities in academia [1], [2], [3], [4], [5], [6] and industry [7], [8], [9]. Yet, to accomplish breakthroughs in dynamic whole-body locomotion, and to robustly traverse unexplored environments, legged robots have to be *terrain aware*. TAL implies that the robot is capable of taking decisions based on the terrain [10]. The decisions can be in planning, control, or in state estimation, and the terrain may vary in its geometry and physical properties [11], [12], [13], [14], [15], [16], [17], [18], [19]. TAL allows the robot to use its onboard sensors to perceive its surroundings and act accordingly. This work is on *vision-based terrain-aware locomotion (ViTAL) planning strategies* that plan the robot’s motion (body and feet) based on the terrain information that is acquired using vision (see Fig. 1).

A. Related Work—Vision-Based Locomotion Planning

Vision-based locomotion planning can either be *coupled* or *decoupled*. The coupled approach jointly plans the body pose and footholds in a single algorithm. The decoupled approach independently plans the body pose and footholds in separate algorithms. The challenge in the coupled approach is that it is computationally expensive to solve in real time. Because of this, the decoupled approach tends to be more practical since the high-dimensional planning problem is split into multiple low-dimensional problems. This also makes the locomotion planning problem more tractable. However, this raises an issue with the decoupled approach because the plans may conflict with each other since they are planned separately. Note that both the approaches could be solved using optimization, learning, or heuristic methods.

TO is one way to deal with coupled vision-based locomotion planning. By casting locomotion planning as an optimal control

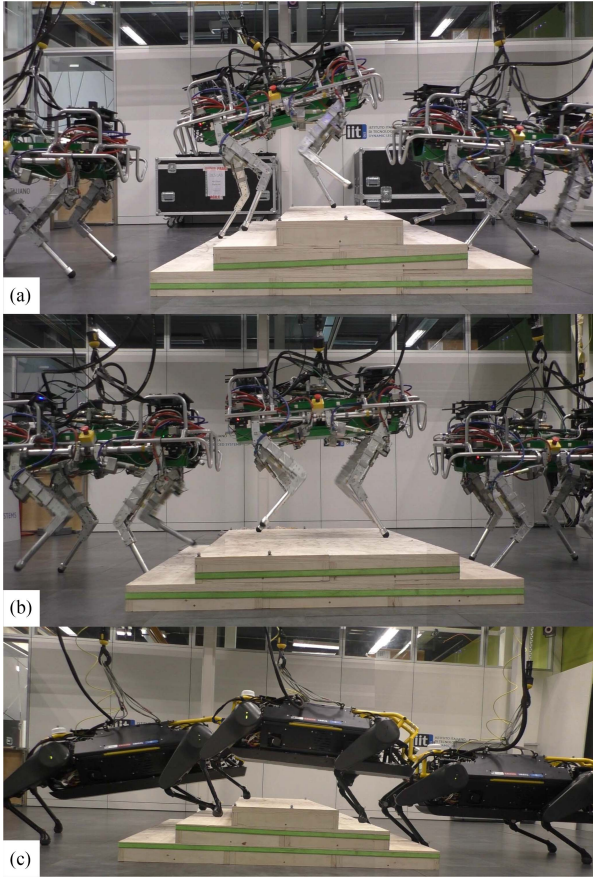


Fig. 1. (a)–(c) HyQ and HyQReal quadruped robots climbing stairs using ViTAL.

problem, TO methods can optimize the robot's motion while taking into account the terrain information [20], [21], [22], [23], [24]. The locomotion planner can generate trajectories that prevent the robot from slipping or colliding with the terrain by encoding the terrain's shape and friction properties in the optimization problem [24]. TO methods can also include a model of the terrain as a cost map in the optimization problem and generate the robot's trajectories based on that [25]. TO methods provide guarantees on the optimality and feasibility of the devised motions, albeit being computationally expensive; performing these optimizations in real time is still a challenge. To overcome this issue, TO approaches often implement hierarchical (decoupled) approaches. Instead of decoupling the plan into body pose and footholds, the hierarchical approaches decouple the plan into short- and long-horizon plans [26], [27]. In addition, other work relies on varying the model complexity to overcome the computational issue with TO [28].

RL methods mitigate the computational burden of TO methods by training function approximators that learn the locomotion plan [29], [30], [31], [32], [33], [34], [35]. Once trained, an RL policy can generate body pose and foothold sequences based on proprioceptive and/or visual information. Yet, RL methods may require tedious learning (large amounts of data and training time) given its high-dimensional state representations.

As explained earlier, decoupled locomotion planning can mitigate the problems of TO and RL by separating the locomotion

plan into feet planning and body planning [36], [37], [38], [39], [40], [41]. Thus, one can develop a more refined and tractable algorithm for every module separately. In this article, planning the feet motion (foothold locations) is called *foothold selection*, and planning the body motion is called *pose adaptation*.

B. Related Work—Foothold Selection and Pose Adaptation

Foothold selection strategies choose the best footholds based on the terrain information and the robot's capabilities. Early work on foothold selection was presented by Kolter et al. [42] and Kalakrishnan et al. [43], where both the approaches relied on motion capture systems and an expert user to select (label) the footholds. These works were then extended in [44] using unsupervised learning, onboard sensors, and considered the terrain information such as the TR (to avoid edges and corners) and friction (to avoid slippage). Then, Barasuol et al. [45] extended the aforementioned work by selecting footholds that considers not only the terrain morphology, but also LCs with the terrain. Further improvements in foothold selection strategies added other evaluation criteria such as the robot's kinematic limits. These strategies use optimization [37], [46], [47], supervised learning [38], [48], [49], RL [1], [17], or heuristic [50] methods.

Similar to foothold selection, pose adaptation strategies optimize the robot's body pose based on the terrain information and the robot's capabilities. An early work on VPA was presented in [36]. The goal was to find the optimal pose that maximizes the reachability of *given* selected footholds, avoid collisions with the terrain, and maintain static stability. The given footholds are based on a foothold selection algorithm that considers the terrain geometry. Another approach was presented in [51] that finds the optimal body elevation and inclination *given* the selected footholds, and the robot location in the map. The pose optimizer maximizes different margins that increase the kinematic reachability of the legs and static stability and avoids terrain collisions. This approach was then extended in [52] with an improved version of the kinematic margins. A similar approach was presented in [37], where the goal was to find an optimal pose that can maximize the reachability of *given* selected footholds. The reachability term is accounted for in the cost function of the optimizer by penalizing the difference between the default foothold position and the selected one. The work in [39] builds on top of the pose optimizer of [37] to adapt the pose of the robot in confined spaces using 3-D terrain maps. This is done using a hierarchical approach that first samples body poses that allows the robot to navigate through confined spaces and, then, smooths these poses using a gradient descent method that is then augmented with the pose optimizer of [37]. The work presented in [53] generates vision-based pose references that also rely on *given* selected footholds to estimate the orientation of the terrain and send it as a pose reference. Alongside the orientation reference, the body height reference is set at a constant vertical distance (parallel to gravity) from the center of the approximated plane that fits through the selected footholds.

The aforementioned pose adaptation strategies focus on finding *one* optimal solution based on *given* footholds; footholds have to be first selected and *given* to the optimizer. Despite selecting footholds that are safe, there are no guarantees on what

would happen during execution if the footholds are not reached or if the robot deviates from its planned motion. If any of these cases happen, the robot might end up in a pose where no safe footholds can be reached. This would, in turn, compromise the safety and performance of the robot. Even if the strategy can replan, reaching a safe pose might not be possible if the robot is already in an unsafe state.

C. Proposed Approach

We propose ViTAL, an online whole-body locomotion planning strategy that consists of a foothold selection and a pose adaptation algorithm. The foothold selection algorithm used in this article is an extension of the VFA algorithm of the previous work done by Villarreal et al. [38] and Esteban et al. [49]. Most importantly, we propose a novel VPA algorithm that introduces a different paradigm to overcome the drawbacks of the state-of-the-art pose adaptation methods. *Instead of finding body poses that are optimal for given footholds, we propose finding body poses that maximize the chances of reaching safe footholds in the first place.* Hence, we are interested in putting the robot in a state in which if it deviates from its planned motion, the robot remains around a set of footholds that are still reachable and safe. The notion of safety emerges from *skills* that characterize the robot's capabilities.

ViTAL plans footholds and body poses by sharing the same robot skills (both for the VPA and the VFA). These skills characterize what the robot is capable of doing. The skills include, but are not limited to the robot's ability to avoid edges, corners, or gaps (*TR*), the robot's ability to remain within the workspace of the legs during the swing and stance phases (*kinematic limits*), and the robot's ability to avoid colliding with the terrain (*LC*). These skills are denoted by *FEC*. Evaluating the FEC is usually computationally expensive. Thus, to incorporate the FEC in ViTAL, we rely on approximating them with CNNs that are trained via supervised learning. This allows us to continuously adapt both the footholds and the body pose. The VFA and the VPA are decoupled and can run at a different update rate. However, they are nonhierarchical, run in parallel, and share the same knowledge of the robot skills (the FEC). By that, we overcome the limitations that result from hierarchical planners, as mentioned in [39], where high-level plans may conflict with the low-level ones causing a different robot behavior.

The VPA utilizes the FEC to approximate a function that provides the number of safe footholds for the legs. Using this function, we cast a *pose optimizer* that solves a nonlinear optimization problem that maximizes the number of safe footholds for all the legs subject to constraints added to the robot pose. The pose optimizer is a key element in the VPA since it adds safety layers and constraints to the learning part of our approach. This makes our approach more tractable, which mitigates the issues that might arise from end-to-end policies in RL methods.

D. Contributions

ViTAL mitigates the abovementioned conflicts that exist in other decoupled planners [37], [39], [41], [46]. This is because both the VPA and the VFA share the same skills encoded in

the FEC. In other words, the VPA and the VFA will not plan body poses and footholds that may conflict with each other because both the planners share the same logic. In this article, the formulation of the VPA allows ViTAL to reason about the leg's capabilities and the terrain information. However, the formulation of the VPA could be further augmented by other body-specific skills. For instance, the VPA could be reformulated to reason about the body collisions with the environment similar to the work in [41] and [54]. The paradigm of the FEC can also be further augmented to consider other skills. We envision that some skills are best encoded via heuristics, while others are well suited through optimization. For this reason, the FEC can also handle optimization-based foothold objectives such as the ones in [46].

Following the recent impressive results in RL-based locomotion controllers, we envision ViTAL to be inserted as a module into such control frameworks. To elaborate, current RL-based locomotion controllers [1], [29], [31], [33] are of a single network; the RL framework is a single policy that maps the observations (proprioceptive and exteroceptive) to the actions. This may be challenging since it requires careful reward shaping, and generalizing to new tasks or different sensors (observations) makes the problem harder [55]. For this reason, and similar to [55], we envision that ViTAL can be utilized as a planner for RL controllers where the RL controller will act as a reactive controller that then receives guided (planned) commands in a form of optimal poses and footholds from ViTAL.

ViTAL differs from TO and optimization-based methods in several aspects. The FEC is designed to independently evaluate every skill (criterion). Thus, one criterion can be optimization based, while other could be using logic or heuristics. Because of this, ViTAL is not restricted by solving an optimization problem that handles all the skills at once. Another difference between ViTAL and TO is in the way the body poses are optimized. In TO, the optimization problem optimizes a single pose to follow a certain trajectory. The VPA in ViTAL optimizes for the body poses that maximizes the chances of the legs in reaching safe footholds. In other words, the VPA finds a body pose that would put the robot in a configuration where the legs have the maximum possible number of safe footholds. In fact, this paradigm that the VPA of ViTAL introduces may also be encoded in TO. In addition, TO often finds body poses that consider the leg's workspace, but to the best of the authors' knowledge, there is no TO method that finds body poses that consider the legs' collision with the terrain and the feasibility of the swinging legs' trajectory.

To that end, the *contributions* of this article are as follows:

- 1) ViTAL, an online vision-based locomotion planning strategy that simultaneously plans body poses and footholds based on the shared knowledge of robot skills (the FEC);
- 2) an extension of our previous work on the VFA algorithm for foothold selection that considers the robot's body twist and the gait parameters;
- 3) a novel pose adaptation algorithm called the VPA that finds the body pose that maximizes the number of safe footholds for the robot's legs.

II. FOOTHOLD EVALUATION CRITERIA

The FEC are main the building block for the VFA and the VPA. The FEC are sets of skills that evaluate footholds within heightmaps. The skills include the robot's ability to assess the terrain's geometry, avoid LCs, and avoid reaching kinematic limits. The FEC can be model based as in this work and [36] and [38], or using optimization techniques as in [37] and [46]. The FEC of this work extends the criteria used in our previous work [38], [45], [49].

The FEC takes a tuple T as an input, evaluates it based on multiple criteria, and outputs a Boolean matrix μ_{safe} . The input tuple T is defined as

$$T = (H, z_h, v_b, \alpha) \quad (1)$$

where $H \in \mathbb{R}^{h_x \times h_y}$ is the heightmap of dimensions h_x and h_y , $z_h \in \mathbb{R}$ is the *hip height* of the leg (in the world frame), $v_b \in \mathbb{R}^6$ is the base twist, and α are the gait parameters (step length, step frequency, duty factor, and time remaining till touchdown). The heightmap H is extracted from the terrain elevation map and is oriented with respect to the horizontal frame of the robot [56]. The horizontal frame coincides with the base frame of the robot, and its xy plane is perpendicular to the gravity vector. Each cell (pixel) of H denotes the terrain height that corresponds to the location of this cell in the terrain map. Each cell of H also corresponds to a *candidate foothold* $p_c \in \mathbb{R}^3$ for the robot.

In this article, we only consider the following FEC: *TR*, *LC*, *KF*, and *FC*. Each criterion C outputs a Boolean matrix μ_C . Once all of the criteria are evaluated, the final output μ_{safe} is the elementwise logical AND (\wedge) of all the criteria. The output matrix $\mu_{\text{safe}} \in \mathbb{R}^{h_x \times h_y}$ is a Boolean matrix with the same size as the input heightmap H . μ_{safe} indicates the candidate footholds (elements in the heightmap H) that are *safe*. An element in the matrix μ_{safe} that is true corresponds to a candidate foothold p_c in the heightmap H that is safe. The output of the FEC is

$$\mu_{\text{safe}} = \mu_{\text{TR}} \wedge \mu_{\text{LC}} \wedge \mu_{\text{KF}} \wedge \mu_{\text{FC}}. \quad (2)$$

An overview of the criteria used in this article is shown in Fig. 2(a) and is detailed as follows.

- 1) *Terrain roughness*: This criterion checks edges or corners in the heightmap that are unsafe for the robot to step on. For each candidate foothold p_c in H , we evaluate the mean and standard deviation of the slope relative to its neighboring footholds and put a threshold that defines whether a p_c is safe or not. Footholds above this threshold are discarded.
- 2) *Leg collision*: This criterion selects footholds that do not result in LC with the terrain during the entire gait cycle (from liftoff, during swinging, touchdown, and till the next liftoff). To do so, we create a bounding region around the leg configuration that corresponds to the candidate foothold p_c and the current hip location. Then, we check if the bounding region collides with the terrain (the heightmap) by measuring the closest distance between them. If this distance is lower than a certain value, then the candidate foothold is discarded.
- 3) *Kinematic feasibility*: This criterion selects footholds that are kinematically feasible. It checks whether a candidate

foothold p_c will result in a trajectory that remains within the workspace of the leg during the entire gait cycle. To do so, we check if the candidate foothold p_c is within the workspace of the leg during touchdown and next liftoff. Also, we check if the trajectory of the foot from the liftoff position p_{lo} till the touchdown position at the candidate foothold p_c is within the workspace of the leg. In the initial implementation in [38], this criterion was only evaluated during touchdown. In this article, we consider this criterion during the entire leg step cycle.

- 4) *Foot trajectory collision*: This criterion selects footholds that do not result in FC with the terrain. It checks whether the foot swing trajectory corresponding to a candidate foothold p_c is going to collide with the terrain or not. If the swing trajectory collides with the terrain, the candidate foothold p_c is discarded.

Remark 1: There are three main sources of uncertainty that can affect the foothold placement [45]. These sources of uncertainty are due to trajectory tracking errors, foothold prediction errors, and drifts in the map. To allow for a degree of uncertainty, after computing μ_{safe} , candidate footholds that are within a radius of unsafe footholds are also discarded. This is similar to the erosion operation in image processing.

Remark 2: The initial implementation of the FEC in [38] only considered the heightmap H as an input; the other inputs of the tuple T in (1) were kept constant. This had a few disadvantages that we reported in [49] where we extended the work of [38] by considering the linear body heading velocity. In this article, we build upon that by considering the full body twist v_b and the gait parameters α as expressed by T in (1).

III. VISION-BASED FOOTHOLD ADAPTATION

The VFA evaluates the FEC to select the optimal foothold for each leg [38], [45], [49]. The VFA has three main stages, as shown in Fig. 2(b): *heightmap extraction*, *foothold evaluation*, and *trajectory adjustment*.

- 1) *Heightmap extraction*: Using the current robot states and gait parameters, we estimate the touchdown position of the swinging foot in the world frame, as detailed in [38]. This is denoted as the *nominal foothold* $p_n \in \mathbb{R}^3$. Then, we extract a heightmap H_{vfa} that is centered around p_n .
- 2) *Foothold evaluation*: After extracting the heightmap, we compute the *optimal foothold* $p_* \in \mathbb{R}^3$ for each leg. We denote this by foothold evaluation, which is the mapping

$$g(T_{\text{vfa}}) : T_{\text{vfa}} \rightarrow p_* \quad (3)$$

that takes an input tuple T_{vfa} that is defined as

$$T_{\text{vfa}} = (H_{\text{vfa}}, z_h, v_b, \alpha, p_n). \quad (4)$$

Once we evaluate the FEC in (2), from all of the safe candidate footholds in μ_{safe} , we select the optimal foothold p_* as the one that is *closest to the nominal* foothold p_n . The aim is to minimize the deviation from the original trajectory and, thus, results in a less disturbed or aggressive motion. An overview of the foothold evaluation stage is shown in Fig. 3, where the tuple T of the FEC in (1) is extracted

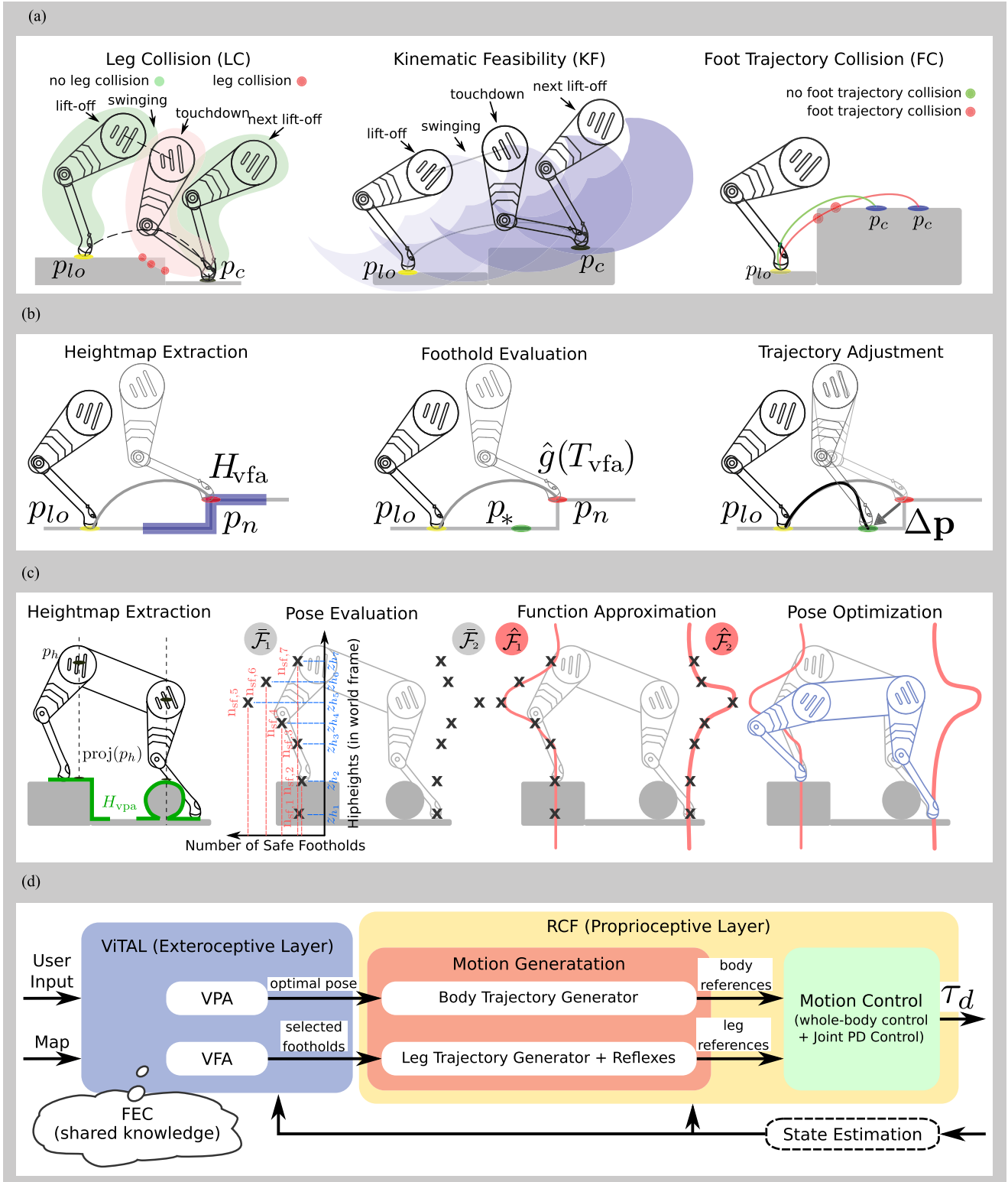


Fig. 2. Overview of ViTAL. Illustrations are not to scale. (a) FEC: LC, KF, and FC. (b) VFA pipeline. First, we extract the heightmap H_{vfa} around the nominal foothold p_n . Then, we evaluate the heightmap either using the exact evaluation $g(T_{vfa})$ or using the CNN as an approximation $\hat{g}(T_{vfa})$. Once the optimal foothold p_* is selected, the swing trajectory is adjusted. (c) VPA pipeline. First, we extract the heightmap H_{vpa} for all the legs. The heightmaps are centered around the projection of the leg hip locations. Then, we evaluate the FEC to compute $\bar{\mathcal{F}}$ for all the hip heights of all the legs (pose evaluation). Then, we approximate a continuous function $\hat{\mathcal{F}}$ from $\bar{\mathcal{F}}$ (function approximation). The pose optimizer finds the pose that maximizes $\hat{\mathcal{F}}$ for all of the legs (pose optimization). (d) Our locomotion framework. ViTAL consists of the VPA and the VFA algorithms. Both the algorithms rely on the robot skills which we denote by the FEC. τ_d are the desired joint torques that are sent to the robot.

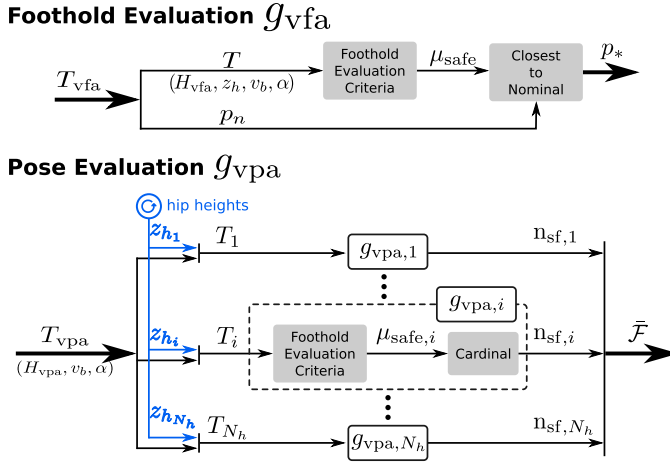


Fig. 3. Overview of the foothold evaluation stage in the VFA algorithm and the pose evaluation stage in the VPA algorithm.

from the VFA tuple T_{vfa} in (4) to compute μ_{safe} . Then, using p_n and μ_{safe} , we extract p_* as the safe foothold that is closest to p_n .

3) *Trajectory adjustment:* The leg's swinging trajectory is adjusted once p_* is computed.

Remark 3: To compute the foothold evaluation, one can directly apply the exact mapping $g(T_{\text{vfa}})$. Yet, computing the foothold evaluation leads to evaluating the FEC, which is generally computationally expensive. Thus, to speed up the computation and to continuously run the VFA online, we train a CNN to approximate the foothold evaluation $\hat{g}(T_{\text{vfa}})$ using supervised learning. Once trained, the VFA can then be executed online using the CNN. The CNN architecture of the foothold evaluation is explained in Appendix A.

IV. VISION-BASED POSE ADAPTATION

The VPA generates pose references that maximize the chances of the legs to reach safe footholds. This means that the robot pose has to be aware of what the legs are capable of and adapt accordingly. Therefore, the goal of the VPA is to adapt the robot pose based on the same set of skills in the FEC used by the VFA.

A. Definitions and Notations

1) *Number of Safe Footholds:* As explained earlier, the FEC takes a tuple T as an input and outputs the matrix μ_{safe} . Based on that, let us define the *number of safe footholds* (n_{sf})

$$n_{\text{sf}} := \text{cardinal}(\{e \in \mu_{\text{safe}} : e = 1\}) \quad (5)$$

as the number of *true* elements in the Boolean matrix μ_{safe} .

2) *Set of Safe Footholds:* Consider a set of tuples \mathcal{T} where each element $T_i \in \mathcal{T}$ is a tuple defined as

$$T_i = (H, z_{h_i}, v_b, \alpha) \quad (6)$$

and $z_{h_i} \in \mathcal{Z}$ is a hip height element in the set of hip heights \mathcal{Z} (in the world frame). All the tuple elements $T_i \in \mathcal{T}$ share the same heightmap H , body twist v_b and gait parameters α .

Evaluating the FEC in (2) for every $T_i \in \mathcal{T}$ that corresponds to $z_{h_i} \in \mathcal{Z}$ and computing the cardinal in (5) yields $n_{\text{sf},i}$ for every T_i . This yields the *set of safe footholds* (\mathcal{F}), which is a set containing the number of safe footholds n_{sf} that are evaluated based on the FEC given the set of tuples \mathcal{T} that corresponds to the set of hip heights \mathcal{Z} but shares the same heightmap H , body twist v_b , and gait parameters α .

B. From the Set of Safe Footholds to Pose Evaluation

The set of safe footholds \mathcal{F} is one of the building blocks of the VPA. To compute \mathcal{F} , we compute the input tuple T_{vpa}

$$T_{\text{vpa}} = (H_{\text{vpa}}, v_b, \alpha) \quad (7)$$

that we then augment with the hip heights z_{h_i} in the hip heights set \mathcal{Z} yielding the set of tuples \mathcal{T} . Then, we evaluate the FEC in (2) for every $T_i \in \mathcal{T}$ and compute the cardinal in (5). This can be expressed by the mapping

$$g_{\text{vpa}}(T_{\text{vpa}}) : T_{\text{vpa}} \rightarrow \mathcal{F} \quad (8)$$

which is referred to as *pose evaluation*. We can express \mathcal{F} as

$$\mathcal{F} = \{n_{\text{sf},i} = g_{\text{vpa},i}(T_i) \forall T_i \in \mathcal{T}\}. \quad (9)$$

Remark 4: Since \mathcal{Z} is an infinite continuous set, so is \mathcal{F} , which is not numerically feasible to compute. Hence, we sample a finite set $\bar{\mathcal{Z}}$ of N_{z_h} samples of hip heights that results in a finite set of safe footholds $\bar{\mathcal{F}}$. To use the set of safe footholds in an optimization problem, we need a continuous function. Thus, after we compute $\bar{\mathcal{F}}$, we estimate a continuous function $\hat{\mathcal{F}}$ as explained next.

An overview of the pose evaluation is shown in Fig. 3, where the tuple T_{vpa} in (7) is augmented with the hip heights z_{h_i} from $\bar{\mathcal{Z}}$ to construct the FEC tuples T_i in (6). For every tuple T_i , we evaluate the FEC using (2) and compute $n_{\text{sf},i}$ in (5) using the mapping in (8). Finally, the set $\bar{\mathcal{F}}$ includes all the elements $n_{\text{sf},i}$ as in (9).

C. VPA Formulation

The VPA has four main stages, as shown in Fig. 2(c): 1) *heightmap extraction* that is similar to the VFA; 2) *pose evaluation* where we compute $\bar{\mathcal{F}}$; 3) *function approximation* where we estimate $\hat{\mathcal{F}}$ from $\bar{\mathcal{F}}$; and 4) *pose optimization* where the optimal body pose is computed.

- 1) *Heightmap extraction:* We extract one heightmap H_{vpa} per leg that is centered around the projection of the leg's hip location in the terrain map ($\text{proj.}(p_h)$ instead of p_n).
- 2) *Pose evaluation:* After extracting the heightmaps, we compute $\bar{\mathcal{F}}$ from the mapping in (8) of the pose evaluation. In the pose evaluation, the FEC are evaluated for all hip heights in $\bar{\mathcal{Z}}$ given the input tuple T_{vpa} , as shown in Fig. 3.
- 3) *Function approximation:* In this stage, we estimate the continuous function $\hat{\mathcal{F}}$ from $\bar{\mathcal{F}}$, as explained in Remark 4. This is done by training a parameterized model of the inputs $T_i \in \bar{\mathcal{T}}$ and the outputs $n_{\text{sf},i} \in \bar{\mathcal{F}}$. The result is the function (model) $\hat{\mathcal{F}}$ that is parameterized by the model parameters w . The function approximation is detailed later in this section.

- 4) *Pose optimization*: Evaluating the FEC and approximating it with the function $\hat{\mathcal{F}}$, introduces a metric that represents the possible number of safe footholds for every leg. Based on this, the goal of the pose optimizer is to find the optimal pose that will maximize the number of safe footholds for every leg (maximize $\hat{\mathcal{F}}$) while ensuring robustness. The pose optimizer is detailed later in this section.

Remark 5: Similar to Remark 3, one can directly apply the exact evaluation $g_{\text{vpa}}(T_{\text{vpa}})$ for a given T_{vpa} . Yet, since this is computationally expensive, we rely on approximating the evaluation $\hat{g}_{\text{vpa}}(T_{\text{vpa}})$ using a CNN. In fact, the learning part is applied to both the pose evaluation and the function approximation. This means that the pose optimization is running online, outside the CNN. The CNN architecture of the pose evaluation is explained in Appendix A.

D. Function Approximation

The goal of the function approximation is to approximate the set of safe footholds \mathcal{F} from the discrete set $\bar{\mathcal{F}}$ computed in the pose evaluation stage. This is done to provide the pose optimizer with a continuous function. Given a dataset $(\bar{\mathcal{Z}}, \bar{\mathcal{F}})$ of hip heights $z_{h_i} \in \bar{\mathcal{Z}}$ and number of safe footholds $n_{sf,i} \in \bar{\mathcal{Z}}$, the function approximation estimates a function $\hat{\mathcal{F}}(z_{h_i}, w)$ that is parameterized by the weights w . Once the weights w are computed, the function estimate $\hat{\mathcal{F}}(z_{h_i}, w)$ is then reconstructed and sent to the pose optimizer.

It is important to choose a function $\hat{\mathcal{F}}$ that can accurately represent the nature of the number of safe footholds. The number of safe footholds approaches zero when the hip heights approach 0 or ∞ . Thus, we want a function that fades to zero at the extremes (Gaussian-like functions) and captures any asymmetry or flatness in the distribution. Hence, we use radial basis functions of Gaussians. With that in mind, we are looking for the weights w

$$w = \arg \min S(w) \quad (10)$$

that minimize the cost $S(w)$

$$S(w) = \sum_{i=1}^{N_h} (n_{sf,i} - \hat{\mathcal{F}}(z_{h_i}, w))^2 \quad (11)$$

which is the sum of the squared residuals of $n_{sf,i}$ and $\hat{\mathcal{F}}(z_{h_i}, w)$. N_h is the number of samples (the number of the finite set of hip heights). The function $\hat{\mathcal{F}}(z_{h_i}, w)$ is the regression model (the approximation of \mathcal{F}) that is parameterized by w . The function $\hat{\mathcal{F}}(z_{h_i}, w)$ is the weighted sum of the basis functions

$$\hat{\mathcal{F}}(z_{h_i}, w) = \sum_{e=1}^E w_e \cdot g(z_{h_i}, \Sigma_e, c_e) \quad (12)$$

where $w \in \mathbb{R}^E$, and E is the number of basis functions. The basis function is a radial basis function of Gaussian functions

$$g(z_{h_i}, \Sigma_e, c_e) = \exp(-0.5(z_{h_i} - c_e)^T \Sigma_e^{-1} (z_{h_i} - c_e)) \quad (13)$$

where Σ_e and c_e are the parameters of the Gaussian function. Since the function model in (12) is linear in the parameters, the weights of the function approximation can be solved analytically

using least squares. In this article, we keep the parameters of the Gaussians (Σ and c) fixed. Hence, the function $\hat{\mathcal{F}}$ is only parameterized by w . For more information on regression with radial basis functions, refer to [57] and Appendix B.

E. Pose Optimization

The pose optimizer finds the robot's body pose u that maximizes the number of safe footholds for all the legs. This is casted as a nonlinear optimization problem. The notion of safe footholds is provided by the function $\hat{\mathcal{F}}(z_h, w)$ that maps a hip height z_h to a number of safe foothold n_{sf} and is parameterized by w . Since the pose optimizer is solving for the body pose u , the function $\hat{\mathcal{F}}(z_h)$ should be encoded using the body pose rather than the hip heights ($\hat{\mathcal{F}} = \hat{\mathcal{F}}(z_h(u))$). This is done by estimating the hip height as a function of the body pose ($z_h = z_h(u)$), as shown in Appendix C.

F. Single-Horizon Pose Optimization

The pose optimization problem is formulated as

$$\underset{u=[z_b, \beta, \gamma]}{\text{maximize}} \quad \mathcal{C}(\hat{\mathcal{F}}_l(z_{h_l}(z_b, \beta, \gamma))) \quad \forall l \in N_l \quad (14)$$

$$\text{subject to} \quad u_{\min} \leq u \leq u_{\max} \quad (15)$$

$$\Delta u_{\min} \leq \Delta u \leq \Delta u_{\max} \quad (16)$$

where $u = [z_b, \beta, \gamma] \in \mathbb{R}^3$ are the decision variables (robot body pose) consisting of the robot height, roll and pitch, respectively, \mathcal{C} is the cost function, $\hat{\mathcal{F}}_l$ is $\hat{\mathcal{F}}$ for every leg l where $N_l = 4$ is the number of legs, $z_{h_l} \in \mathbb{R}$ is the hip height of the leg l , and u_{\min} and u_{\max} are the lower and upper bounds of the decision variables, respectively. $\Delta u = u - u_{k-1}$ is the numerical difference of u , where u_{k-1} is the output of u at the previous instant, and Δu_{\min} and Δu_{\max} are the lower and upper bounds of Δu , respectively. We can rewrite (16) as

$$\Delta u_{\min} + u_{k-1} \leq u \leq \Delta u_{\max} + u_{k-1}. \quad (17)$$

The cost function in (14) maximizes $\hat{\mathcal{F}}$ for all of the legs. We designed several types of cost functions, as detailed next. The constraints in (15) and (16) ensure that the decision variables and their variations are bounded.

G. Cost Functions

A standard cost function can be the sum of the squares of $\hat{\mathcal{F}}_l$ for all of the legs

$$\mathcal{C}_{\text{sum}} = \sum_{l=1}^{N_l=4} \|\hat{\mathcal{F}}_l(z_{h_l})\|_Q^2 \quad (18)$$

where another option could be the product of the squares of $\hat{\mathcal{F}}_l$ for all of the legs

$$\mathcal{C}_{\text{prod}} = \prod_{l=1}^{N_l=4} \|\hat{\mathcal{F}}_l(z_{h_l})\|_Q^2. \quad (19)$$

The key difference between an additive cost \mathcal{C}_{sum} and a multiplicative cost $\mathcal{C}_{\text{prod}}$ is that the latter puts equal weighting for

each $\hat{\mathcal{F}}_l$. This is important since we do not want the optimizer to find a pose that maximizes $\hat{\mathcal{F}}$ for one leg while compromising the other leg(s). One can also define the cost

$$\mathcal{C}_{\text{int}} = \sum_{l=1}^{N_l=4} \left\| \int_{z_{h_l}-m}^{z_{h_l}+m} \hat{\mathcal{F}}_l(z_{h_l}) dz_{h_l} \right\|_Q^2 \quad (20)$$

which is the *sum of squared integrals* that can be numerically approximated as

$$\int_{z_{h_l}-m}^{z_{h_l}+m} \hat{\mathcal{F}}_l(z_{h_l}) dz_{h_l} \approx m \cdot (\hat{\mathcal{F}}_l(z_{h_l} - m) + \hat{\mathcal{F}}_l(z_{h_l} + m)) \quad (21)$$

yielding

$$\mathcal{C}_{\text{int}} = \sum_{l=1}^{N_l=4} \left\| m \cdot (\hat{\mathcal{F}}_l(z_{h_l} - m) + \hat{\mathcal{F}}_l(z_{h_l} + m)) \right\|_Q^2. \quad (22)$$

In this cost option, we do not find the pose that maximizes $\hat{\mathcal{F}}$. Instead, we want to find the pose that maximizes the area around $\hat{\mathcal{F}}$ that is defined by the margin m . Using \mathcal{C}_{int} is important since it adds robustness in case there is any error in the pose tracking during execution. Because of possible tracking errors during execution, the robot might end up in the pose $u^* \pm m$ instead of u^* . If we use \mathcal{C}_{int} as a cost function, the optimizer will find poses that maximize the number of safe footholds not just for u^* but within a vicinity of m . More details on the use of \mathcal{C}_{int} as a cost function in the pose optimization of the VPA can be found in Appendix D.

H. Receding-Horizon Pose Optimization

Adapting the robot's pose during dynamic locomotion requires reasoning about what is ahead of the robot: the robot should not just consider its current state but also future ones. For that, we extend the pose optimizer to consider the current and future states of the robot in a receding horizon manner. To formulate the receding horizon pose optimizer, instead of considering $\hat{\mathcal{F}}_l \forall l \in N_l$ in the single horizon case, the pose optimizer will consider $\hat{\mathcal{F}}_{l,j} \forall l \in N_l, j \in N_h$, where N_h is the receding horizon number. We compute $\hat{\mathcal{F}}_{l,j}$ in the same way explained in the pose evaluation stage. More details on computing $\hat{\mathcal{F}}_{l,j}$ can be found in Appendix E.

The receding horizon pose optimization problem is

$$\begin{aligned} & \underset{u=[u_1^T, \dots, u_{N_h}^T]}{\text{maximize}} && \sum_{j=1}^{N_h} \mathcal{C}_j(\hat{\mathcal{F}}_{l,j}(z_{h_{l,j}}(u_j))) \\ & + && \sum_{j=1}^{N_h-1} \|u_j - u_{j+1}\| \\ & && \forall l \in N_l, j \in N_h \end{aligned} \quad (23)$$

$$\text{subject to} \quad u_{\min} \leq u \leq u_{\max} \quad (24)$$

$$\Delta u_{\min} \leq \Delta u \leq \Delta u_{\max} \quad (25)$$

where $u = [u_1^T, \dots, u_j^T, \dots, u_{N_h}^T] \in \mathbb{R}^{3N_h}$ are the decision variables during the entire receding horizon N_h . Each variable $u_j = [z_{b,j}, \beta_j, \gamma_j] \in \mathbb{R}^3$ is the optimal pose of the horizon j .

The first term in (23) is the sum of the cost functions \mathcal{C}_j during the entire horizon ($\forall j \in N_h$). The cost \mathcal{C}_j can be any of the aforementioned cost functions. The second term in (23) penalizes the deviation between two consecutive optimal poses within the receding horizon (u_j and u_{j+1}). The second term is added so that each optimal pose u_j is also taking into account the optimal pose of the upcoming sequence u_{j+1} (to connect the solutions in a smooth way). Similar to the single horizon pose optimizer, u_{\min} and u_{\max} are the lower and upper bounds of the decision variables, respectively. Furthermore, Δu denotes the numerical difference of u , while Δu_{\min} and Δu_{\max} are the lower and upper bounds of Δu , respectively. Note that the constraints of the single horizon and the receding horizon are of different dimensions.

V. SYSTEM OVERVIEW

Our locomotion framework that is shown in Fig. 2(d) is based on the RCF [56]. ViTAL complements the RCF with an exteroceptive terrain-aware layer composed of the VFA and the VPA. ViTAL takes the robot states, the terrain map, and user commands as inputs and sends out the selected footholds and body pose to the RCF (perceptive) layer. The RCF takes the robot states and the references from ViTAL and uses them inside a motion generation and a motion control block. The motion generation block generates the trajectories of the leg and the body and adjusts them with the reflexes from [56], [58]. The legs and body references from the motion generation block are sent to the motion control block. The motion control block consists of a WBC [59] that generates desired torques that are tracked via a low-level torque controller [60] and sent to the robot's joints. The framework also includes a state estimation block that feeds back the robot states to each of the aforementioned layers [61]. More implementation details on ViTAL and the entire framework are in Appendix F.

We demonstrate ViTAL on the 90-kg HyQ and the 140-kg HyQReal quadruped robots. Each leg of the two robots has three degrees of freedom (three actuated joints). The torques and angles of the 12 joints of both the robots are directly measured. The bodies of HyQ and HyQReal have a tactical-grade inertial measurement unit (IMU) (KVH 1775). More information on HyQReal and HyQ can be found in [3] and [62], respectively.

We noticed a significant drift in the states of the robots in experiment. To tackle this issue, the state estimator fused the data from a motion capture system and the IMU. This reduced the drift in the base states of the robots albeit not eliminating it completely. Improving the state estimation is an ongoing work and is out of the scope of this article. We used the grid map interface [63] to get the terrain map in simulation. Owing to the issues with state estimation on the real robots, we constructed the grid map before the experiments and used the motion capture system to locate the map with respect to the robot.

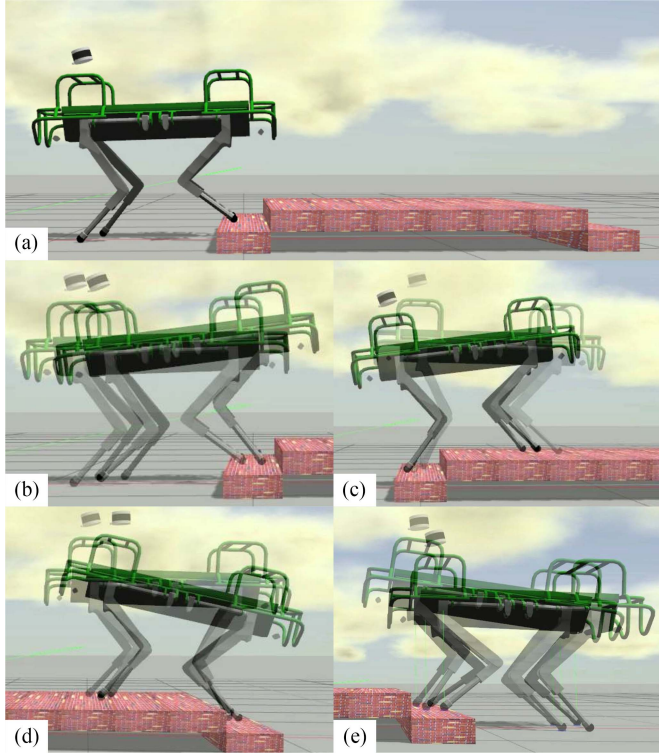


Fig. 4. HyQ climbing stairs in simulation. (a) Full scenario. (b) Robot pitches up to allow for safe footholds for the front legs. (c) Robot lifts up the hind hips to avoid hind LCs with the step. (d) Robot pitches down to allow for safe footholds for the front legs. (e) Robot lowers the hind hips to allow for safe footholds for the legs when stepping down.

VI. RESULTS

We evaluate ViTAL on HyQ and HyQReal. We consider all the FEC mentioned earlier for the VFA and the VPA. We use the receding horizon pose optimizer of (25) and the sum of squared integral of (22). We choose stair climbing as an application for ViTAL. Climbing stairs is challenging for HyQ due to its limited leg workspace in the sagittal plane. Videos associated with the upcoming results can be found in the supplementary materials and [64]. Finally, an analysis of the accuracy of the CNNs and the computational time of ViTAL can be found in Appendixes G and H, respectively.

A. Climbing Stairs (Simulation)

We carried out multiple simulations where HyQ is climbing the stairs shown in Fig. 4. Each step has a rise of 10 cm and a go of 25 cm. HyQ is commanded to trot with a desired forward velocity of 0.2 m/s using the VPA and the VFA. Fig. 4 shows screenshots of one simulation run, and Video 1 shows three simulation runs.

Fig. 4 shows the ability of the VPA in adapting the robot pose to increase the chances of the legs to succeed in finding a safe foothold. In Fig. 4(b), HyQ raised its body and pitched upward so that the front hips are raised to increase the workspace of the front legs when stepping up. In Fig. 4(c), HyQ raised its body and pitched downward so that the hind hips are raised. This is done for two reasons: first, to have a larger clearance between

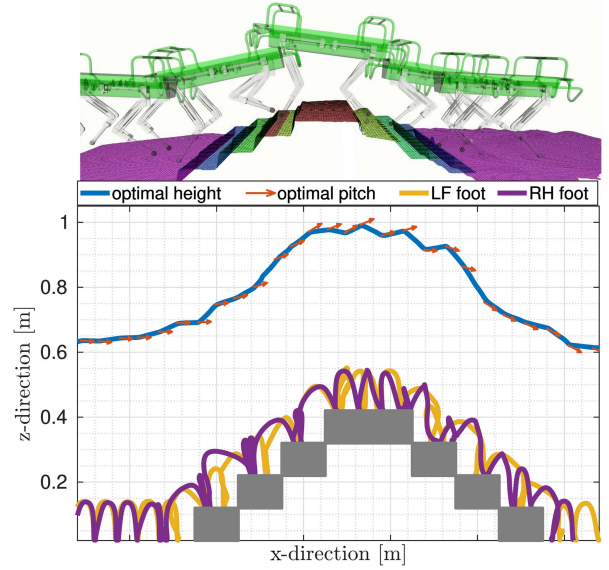


Fig. 5. Climbing stairs: a more complex scenario. Top: Overlaid screenshots of HyQ climbing stairs. Bottom: the optimal height and corresponding pitch (presented by the arrows) and the foot trajectories of LF and RH legs.

the hind legs and the obstacle and, thus, avoid LC with the edge of the stairs; second, to increase the workspace of the hind legs when stepping up and, thus, avoid reaching the workspace limits and collisions along the foot swing trajectory. In Fig. 4(d), HyQ lowered its body and pitched downward so that the front hips are lowered. This is done for two reasons: first, to increase the workspace of the front legs when stepping down and, thus, avoid reaching the workspace limits; second, to have a larger clearance between the front legs and the obstacle and, thus, avoid LCs. In Fig. 4(e), HyQ lowered its hind hips to increase the hind legs' workspace when stepping down.

Throughout these simulations, the robot continuously adapted its body pose and its feet to find the best tradeoff between increasing the KF and avoiding trajectory and LC. This can be seen in Video 1, where the robot's legs and the corresponding feet trajectories never collided with the terrain. The robot took multiple steps around the same foot location before stepping over an obstacle. The reason behind this is that the robot waited for the VPA to change the pose and allow for safe footholds, and then, the VFA took the decision of stepping over the obstacle.

We carried out another scenario where HyQ is climbing the stairs setup in Fig. 5, where each step has a rise of 10 cm and a go of 25 cm. HyQ is commanded to trot with a desired forward velocity of 0.2 m/s using ViTAL. The results are reported in Fig. 5 and Video 2. Fig. 5 shows the robot's height and pitch based on the VPA and the corresponding foot trajectories of the LF leg and the RH leg based on the VFA. HyQ's behavior was similar to the previous section: it accomplished the task without collisions or reaching workspace limits.

B. Climbing Stairs (Experiments)

To validate ViTAL in experiments, we created three sets of experiments using the setups shown in Fig. 1. Each step has a rise of 10 cm and a go of 28 cm.

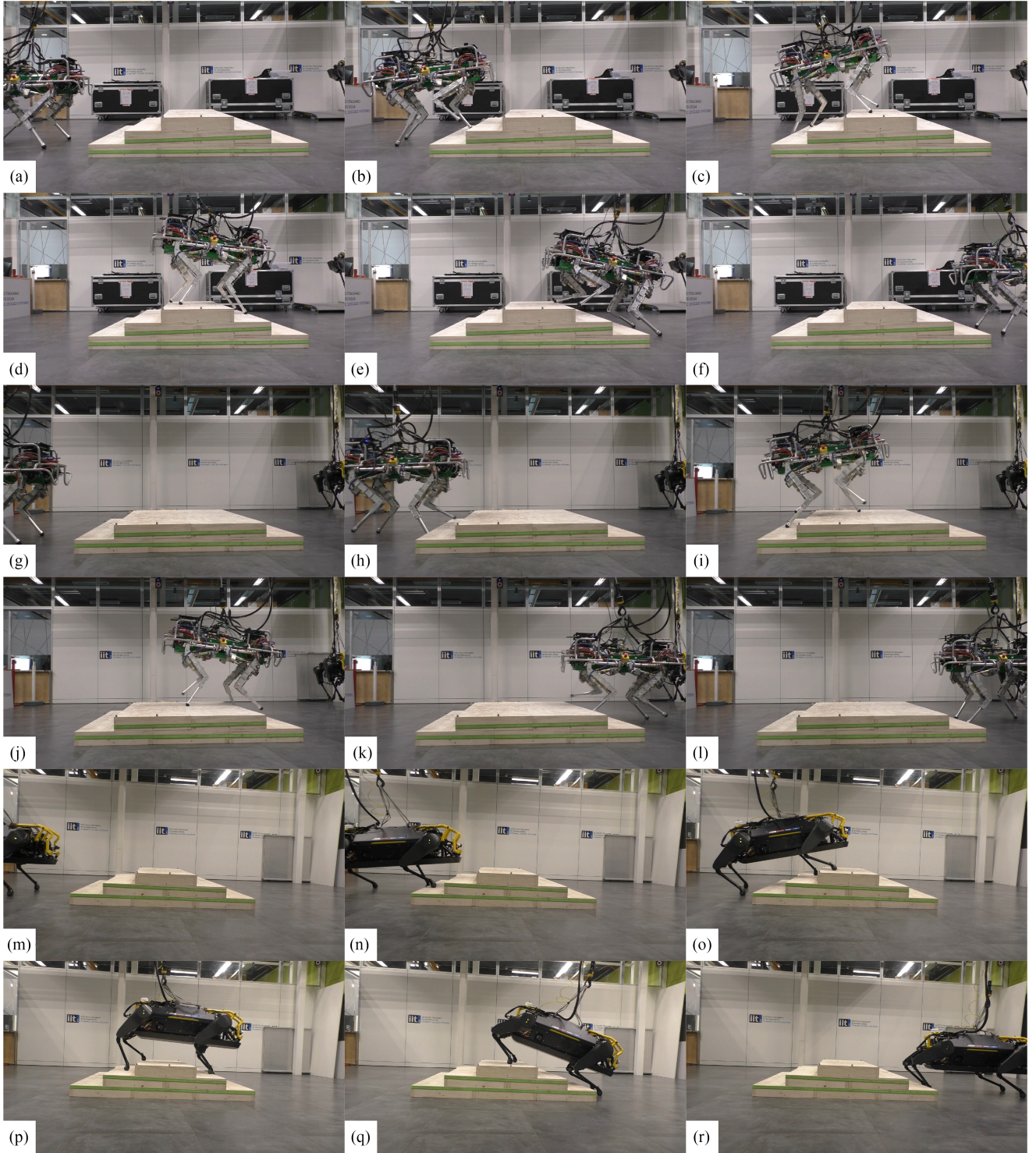


Fig. 6. HyQ and HyQReal climbing stairs in the experiment. (a)–(f) HyQ crawling over with 0.1-m/s commanded forward velocity. (g)–(l) HyQ trotting over with 0.25-m/s commanded forward velocity. (m)–(r) HyQReal crawling over with 0.2-m/s commanded forward velocity.

In the first set of experiments, HyQ is commanded to crawl over the setups in Fig. 1(a) and (b) with a desired forward velocity of 0.1 m/s using the VPA and the VFA. Fig. 6(a)–(f) shows screenshots of one trial. Video 3 shows HyQ climbing back and forth the setup in Fig. 1(b) five times. Video 4 shows HyQ climbing the setup shown in Fig. 1(a), which is reported in Fig. 7. Fig. 7 shows the robot's height and pitch based on

the VPA, and the corresponding feet trajectories of the left-front (LF) leg and the right-hind (RH) leg based on the VFA. This set of experiments confirms that ViTAL is effective on the real platform. The robot managed to accomplish the task without collisions or reaching workspace limits.

In the second set of experiments, HyQ is commanded to trot over the setup in Fig. 1(b) with a desired forward velocity

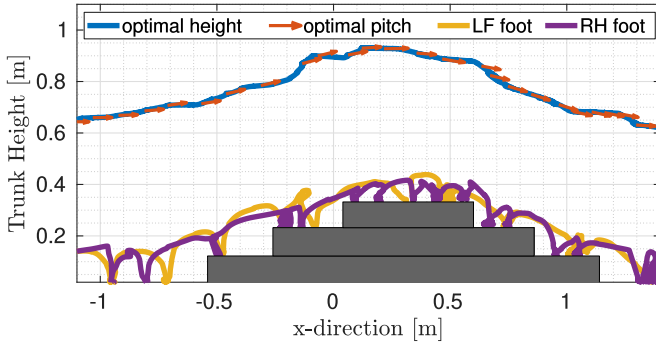


Fig. 7. HyQ climbing stairs in the experiment. The figure shows the optimal height and corresponding pitch (presented by the arrows) based on the VPA, and the foot trajectories of the LF and RH legs based on the VFA.

TABLE I
MEAN ABSOLUTE TRACKING ERRORS OF THE BODY PITCH β AND HEIGHT z_b OF HYQ AND HYQREAL USING ViTAL IN THE EXPERIMENTS DETAILED IN SECTION VI-B AND IN FIG. 1

Description	β [degree]	z_b [cm]
Exp. (A): HyQ crawling at 0.1 m/s	1.0	1.5
Exp. (B): HyQ trotting at 0.2 m/s	1.0	2.3
Exp. (C): HyQReal crawling at 0.2 m/s	1.0	4.2

of 0.25 m/s using the VPA and the VFA. Fig. 6(g)–(l) shows separate screenshots of this trial. Video 5 shows three trials of HyQ climbing the same setup. This set of experiments shows that ViTAL can handle different gaits.

Finally, in the third set of experiments, HyQReal is commanded to crawl over the setup in Fig. 1(c) with a desired forward velocity of 0.2 m/s using the VPA and the VFA. The results are reported in Fig. 6(m)–(r) that shows screenshots of this trial. Video 6 shows HyQReal climbing this stair setup [see Fig. 1(c)]. This set of experiments shows that ViTAL can work on different legged platforms.

The tracking performance of these three sets of experiments is shown in Table I. The table shows the mean absolute tracking errors of the body pitch β and height z_b of HyQ and HyQReal.

C. Climbing Stairs With Different Forward Velocities

We evaluate the performance of HyQ under different commanded velocities using ViTAL. We carried out a series of simulations using the stairs setup shown in Fig. 5. HyQ is commanded to trot at four different forward velocities: 0.2 m/s, 0.3 m/s, 0.4 m/s, and 0.5 m/s. The results are reported in Fig. 8 and in Video 7. In addition, the tracking performance of these series of simulations at the four different forward velocities is shown in Table II. The table shows the mean absolute tracking errors of the body pitch β and height z_b of HyQ at the corresponding commanded forward velocity. Fig. 8 shows the numerical differences Δz_b and $\Delta \gamma$ and the tracking errors of the body height and pitch, respectively.

HyQ was able to climb the stairs terrain under different commanded velocities. However, as the commanded velocity increases, HyQ started having faster (abrupt) changes in the body

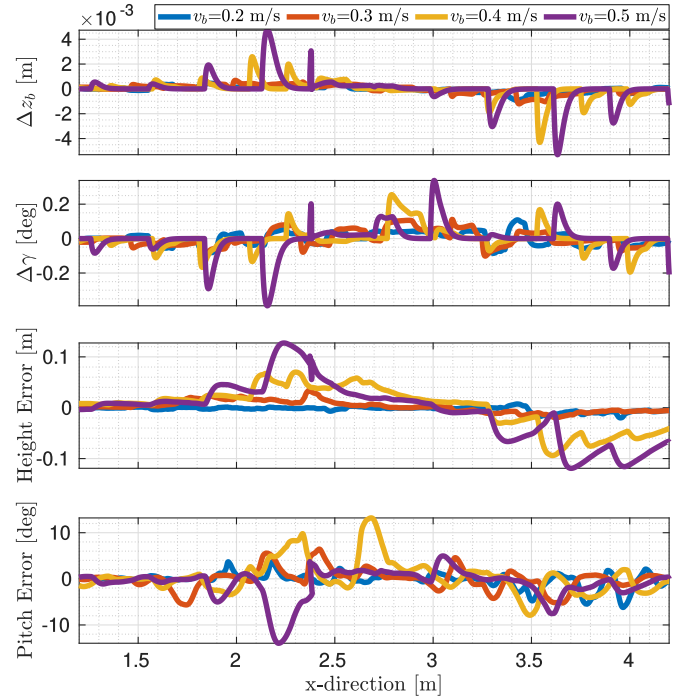


Fig. 8. HyQ's performance using ViTAL under different commanded velocities. The top two plots show the numerical difference of the body height and pitch (Δz_b and $\Delta \gamma$), and the bottom two plots show the tracking errors of the body height and pitch.

TABLE II
MEAN ABSOLUTE TRACKING ERRORS OF THE BODY PITCH β AND HEIGHT z_b OF HYQ USING ViTAL IN SIMULATION WITH DIFFERENT FORWARD VELOCITIES AS DETAILED IN SECTION VI-C AND FIG. 8

Description	β [degree]	z_b [cm]
Sim. (A): HyQ trotting at 0.2 m/s	0.7	0.3
Sim. (B): HyQ trotting at 0.3 m/s	1.1	0.7
Sim. (C): HyQ trotting at 0.4 m/s	2.3	2.6
Sim. (D): HyQ trotting at 0.5 m/s	1.6	3.8

pose, as shown in the top two plots of Fig. 8. As a result, the height and pitch tracking errors increase proportionally to the commanded speed, as shown in the bottom two plots of Fig. 8. This can also be seen in Table II, where the mean absolute tracking errors of the pitch and height increase proportionally to the commanded speed.

Similarly to HyQ, we evaluate ViTAL on HyQReal and commanded it to trot with five different forward velocities: 0.2 m/s, 0.3 m/s, 0.4 m/s, 0.5 m/s, and 0.75 m/s. We report this simulation in Video 8 where we show that ViTAL is robot independent. Yet, since the workspace of HyQReal is larger than HyQ, this scenario was more feasible to traverse for HyQReal. Thus, HyQReal was able to reach a higher commanded velocity than the ones reported for HyQ.

D. Comparing the VPA With a Baseline (Experiments)

We compare the VPA with another VPA strategy: the TBR [38]. The TBR generates pose references based on the

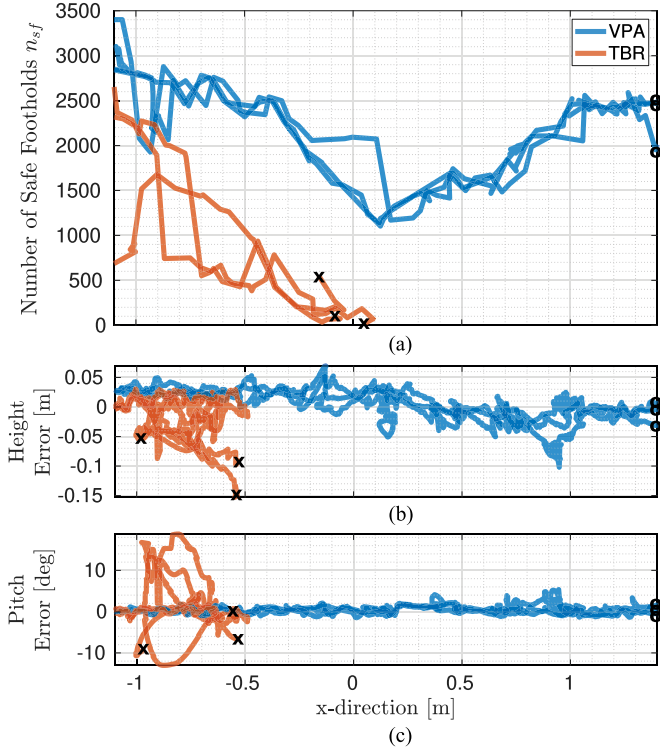


Fig. 9. Difference between the VPA and the TBR in six experiments (three each). (a) Number of safe footholds corresponding to the robot pose. (b) and (c) Body height and pitch tracking errors, respectively. Circles (o) and crosses (x) are successful and failed trials, respectively. Unlike the VPA, the TBR failed to climb the stairs because the TBR resulted in almost no safe footholds for the four legs to reach.

footholds selected by the VFA. The TBR fits a plane that passes through the given selected footholds and sets the orientation of this plane as a body orientation reference to the robot. The elevation reference of the TBR is a constant distance from the center of the approximated plane that passes through the selected footholds. We chose the TBR instead of an optimization-based strategy since the latter does not provide references that are fast enough with respect to the VPA.

Using the stairs setup in Fig. 1(a), we conducted six experimental trials: three with the VPA and three with the TBR. All trials were with the VFA. In all the trials, HyQ is commanded to crawl with a desired forward velocity of 0.1 m/s. The results are reported in Fig. 9 and Video 9. Fig. 9(a) shows the number of safe footholds corresponding to the robot pose from the VPA and the TBR. The robot height and pitch tracking errors are shown in Fig. 9(b) and (c), respectively.

As shown in Video 9, HyQ failed to climb the stairs with the TBR, while it succeeded with the VPA. This is because, unlike the VPA, the TBR does not aim to put the robot in a pose that maximizes the chances of the legs to succeed in finding safe footholds. As shown in Fig. 9(a), the number of safe footholds from using the TBR was below the ones from using the VPA. During critical periods when the robot was around 0 m in the x -direction, the number of safe footholds from using the TBR almost reached zero. The low number of

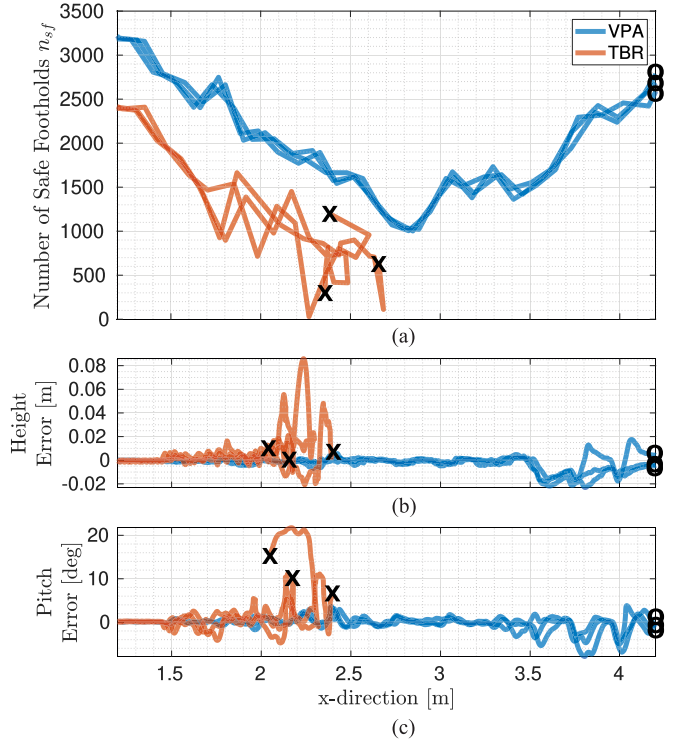


Fig. 10. Difference between the VPA and the TBR in six simulations (three each). (a) Number of safe footholds corresponding to the robot pose. (b) and (c) Body height and pitch tracking errors, respectively. Circles (o) and crosses (x) are successful and failed trials, respectively. Unlike the VPA, the TBR failed to climb the stairs because the TBR resulted in almost no safe footholds for the four legs to reach.

safe footholds for the TBR compared to the VPA is reflected in the tracking of the robot height and pitch, as shown in Fig. 9(b) and (c), where the tracking errors from the TBR were higher than the VPA.

The difference between the VPA and the TBR can be further explained in Video 9. When the TBR is used, the robot is adapting its pose *given* the selected foothold. However, if the selected foothold is not reached, or if there is a high tracking error, the robot reaches a body pose that results in a smaller number of safe footholds. Thus, the feet end up colliding with the terrain, and hence, the robot falls. On the other hand, the VPA is able to put the robot in a pose that maximizes the number of safe footholds. As a result, the feet found alternative safe footholds to select from, which resulted in no collision, and succeeded in climbing the stairs. The VPA optimizes for the number of safe footholds. Thus, if there is a variation around the optimal pose (tracking error), the VFA still finds more footholds to step on, which is not the case with the TBR.

E. Comparing the VPA With a Baseline (Simulation)

Similar to experiments, and using the stairs setup in Fig. 5, we compare the VPA with the TBR. We conducted six simulations: three with the VPA and three with the TBR. All the trials were with the VFA. In all the trials, HyQ is commanded to trot with a 0.2-m/s desired forward velocity. The results are reported in Fig. 10 and Video 10. Fig. 10(a) shows the number of safe

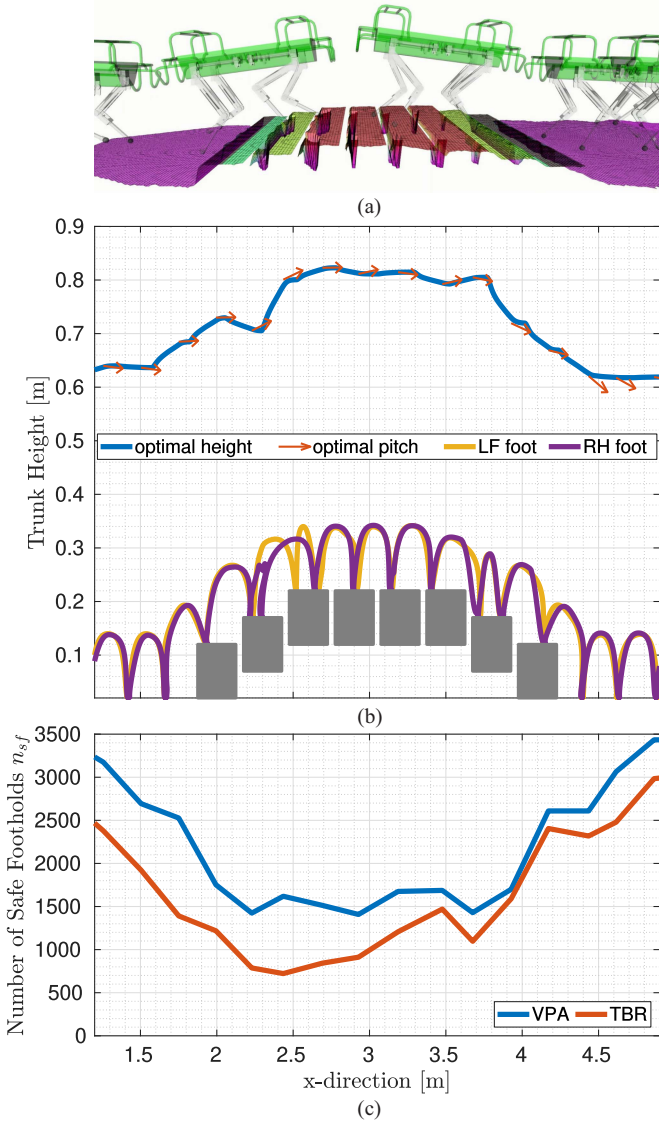


Fig. 11. HyQ climbing gapped stairs. (a) Screenshots of HyQ climbing the setup. (b) Robot's height and pitch based on the VPA, and the corresponding feet trajectories of the LF and RH legs based on the VFA. (c) Number of safe footholds using the VPA and the TBR.

footholds corresponding to the robot pose from the VPA, and the TBR. The tracking errors of the robot height and pitch are shown in Fig. 10(b) and (c), respectively. These trials show that HyQ failed to climb the stairs using the TBR, while it succeeded using the VPA.

F. Climbing Stairs With Gaps

We show HyQ's capabilities of climbing stairs with gaps using ViTAL, and we compare the VPA with the TBR. In this scenario, HyQ is commanded to trot at 0.4 m/s. Fig. 11(a) shows overlaid screenshots of the simulation and the used setup. Fig. 11(b) shows the robot's height and pitch based on the VPA, and the corresponding feet trajectories of the LF leg and the RH leg based on the VFA, and Fig. 11(c) shows the number of safe footholds using the VPA and the TBR. Because of ViTAL, HyQ was able

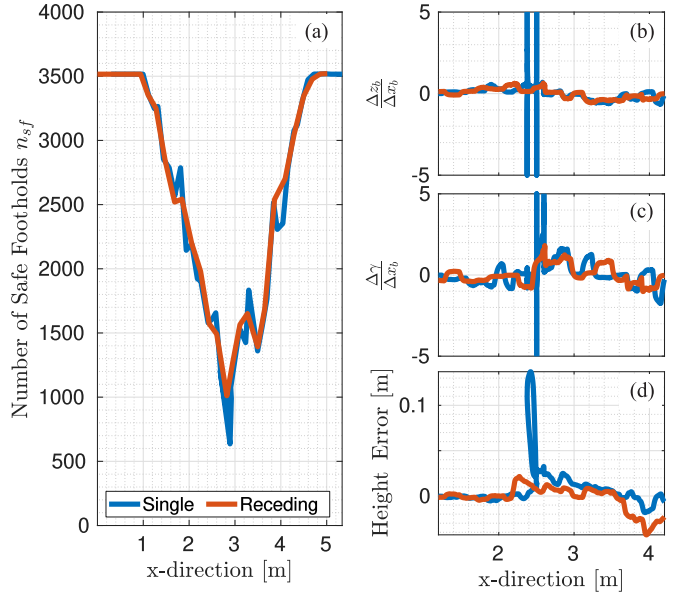


Fig. 12. Pose optimization: single versus receding horizons. (a) Number of safe footholds. (b) Variation (numerical difference) of the robot's height. (c) Variation (numerical difference) of the robot's pitch. (d) Tracking error of the robot's height.

to climb the stairs with gaps while continuously adapting its pose and feet. Furthermore, the number of safe footholds from using the TBR is always lower than from using the VPA, which shows that indeed the VPA outperforms the TBR. Video 11 shows the output of this simulation using ViTAL.

G. Pose Optimization: Single Versus Receding Horizons

To analyze the differences between the receding horizon and the single horizon in pose optimization, we use the stairs setup in Fig. 5 with a commanded forward velocity of 0.4 m/s and report the outcome in Fig. 12 and Video 12. The main advantage of using a receding horizon instead of a single horizon is that the pose optimization can consider future decisions. Thus, if the robot is trotting at higher velocities, the pose optimizer can adapt the robot's pose beforehand. This can result in a better adaptation strategy with less variations in the generated optimal pose. Thus, we analyze the two approaches by taking a look at the variations in the body pose

$$\dot{z}_b = \frac{\Delta z_b}{\Delta x_b} \quad \text{and} \quad \dot{\gamma} = \frac{\Delta \gamma}{\Delta x_b} \quad (26)$$

where \dot{z}_b and $\dot{\gamma}$ are the numerical differences (variations) of the robot height z_b and pitch γ with respect to the robot forward position x_b , respectively.

Fig. 12 reports the differences between the two cases. The number of safe footholds is shown in Fig. 12(a). The variations in \dot{z}_b and $\dot{\gamma}$ are shown in Fig. 12(b) and (c), respectively. Finally, the tracking error of the robot's height is shown in Fig. 12(d). As shown in Fig. 12, the receding horizon resulted in less variations in the body pose compared to the single horizon. This resulted in a smaller tracking error for the receding horizon in the body height, which resulted in slightly larger number of safe

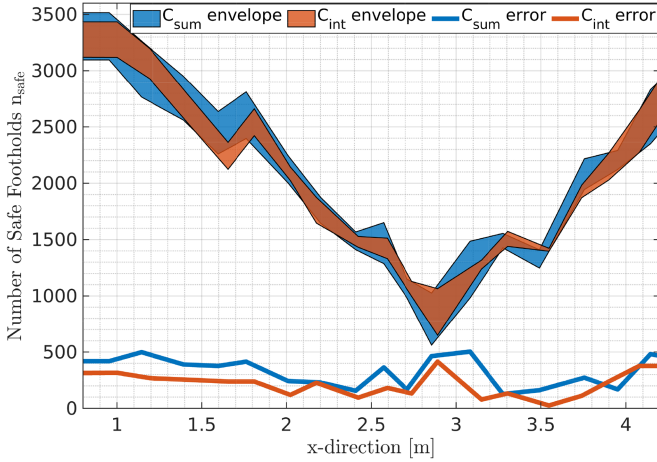


Fig. 13. Pose optimization: C_{sum} versus C_{int} . The shaded areas are the envelopes of the number of safe footholds. The lines are the thicknesses (errors) between these envelopes.

footholds. All in all, the receding horizon reduces variations in the desired trajectories, which improves the trajectory tracking response.

The differences between the receding and single horizon in the pose optimization can also be noticed in Video 12. In the case of a single horizon, the robot was struggling while climbing up the stairs but was able to recover and accomplish the task. However, using the receding horizon, the robot was able to adapt its pose in time, thus resulting in safer footholds that allowed the robot to accomplish the task.

H. Pose Optimization: C_{sum} Versus C_{int}

To analyze the differences between C_{sum} and C_{int} in the pose optimization, we use the stairs setup in Fig. 5 with a commanded forward velocity of 0.4 m/s and report the outcome in Fig. 13. The main advantage of using C_{int} over C_{sum} is that C_{int} will result in a pose that does not just maximize the number of safe footholds for all of the legs, but also ensures that the number of safe footholds of the poses around the optimal pose is still high. To compare the two cost functions, we take a look at the number of safe footholds. In particular, we evaluate the number of safe footholds corresponding to the optimal pose and the poses around it with a margin of $m = 0.025$ m. Thus, in Fig. 13, we plot the envelope (shaded area) between $\hat{\mathcal{F}}(u^* + m)$ and $\hat{\mathcal{F}}(u^* - m)$ for both the cases and the thickness between these envelopes which we refer to as error

$$\text{error} = |\hat{\mathcal{F}}(u^* + m) - \hat{\mathcal{F}}(u^* - m)|. \quad (27)$$

As shown in Fig. 13, the envelope of the number of safe footholds resulting from C_{int} is almost always encapsulated by C_{sum} . The thickness (error) of the number of safe footholds resulting from using C_{int} is always smaller than C_{sum} . This means that any variation of m in the optimal pose will be less critical if C_{int} is used compared to C_{sum} .

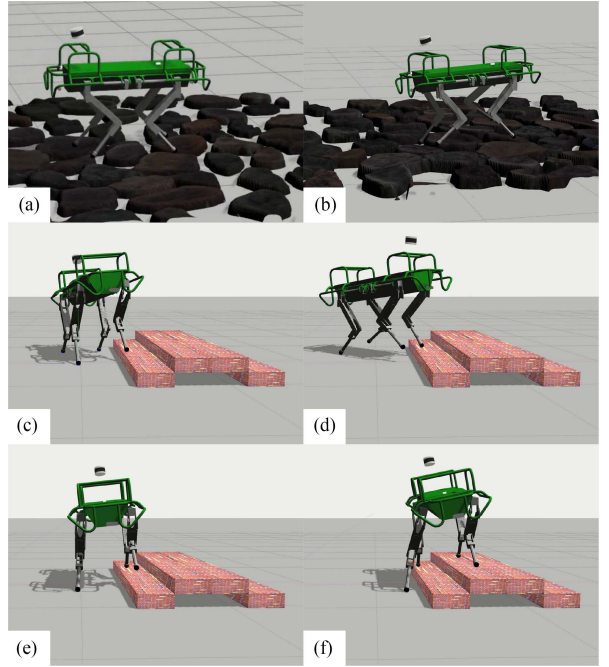


Fig. 14. HyQ traversing rough terrain and climbing stairs sideways. (a) and (b) HyQ traversing rough terrain with and without ViTAL, respectively. (c) and (d) HyQ climbing stairs while yawing (commanding the yaw rate) using ViTAL. (e) and (f) HyQ climbing stairs sideways using ViTAL.

I. Locomotion Over Rough Terrain

We evaluate the performance of HyQ in traversing rough terrain, as shown in Fig. 14(a) and (b) and in Video 13. We conducted two simulations: one with ViTAL and thus with exteroceptive and proprioceptive reactions [see Fig. 14(a)], and another without ViTAL and thus only with proprioceptive reactions [see Fig. 14(b)]. HyQ was commanded to traverse the rough terrain with a forward velocity of 0.2 m/s. No hyperparameters' retuning or CNNs' retraining were needed.

As shown in Video 13, HyQ was able to successfully traverse the terrain in both the cases. With ViTAL, HyQ collided less with the terrain and continuously adapted its footholds over the small cobblestones. Without ViTAL, HyQ traversed the rough terrain, yet, with significantly more effort. In addition, without ViTAL, HyQ continuously collided with the terrain, and in some incidents, the feet got stuck. For this reason, we had to retune the gait parameters and increase the step height to reduce these incidents. The robot's feet also kept slipping since the feet were always close to edges and corners.

J. Climbing Stairs With Different Commands

Instead of commanding only forward velocities as in the previous sections, we command HyQ to climb the stairs with ViTAL while yawing (commanding the yaw rate), as shown in Video 14 and Fig. 14(c) and (d), and to climb stairs laterally, as shown in Video 15 and Fig. 14(e) and (f). Climbing stairs sideways is more challenging than facing the stairs since the range of motion of the robot's roll orientation is more restricted versus the pitch orientation. That said, because of ViTAL, HyQ was still

able to climb these stairs in both the cases, as shown in videos 14 and 15.

VII. CONCLUSION

In this article, we presented ViTAL, which is an online vision-based locomotion planning strategy. ViTAL consists of the VPA for pose adaptation and the VFA for foothold selection. The VPA introduces a different paradigm to current state-of-the-art pose adaptation strategies. The VPA finds body poses that maximize the chances of the legs to succeed in reaching safe footholds. This notion of success emerges from the robot's skills. These skills are encapsulated in the FEC that include (but are not limited to) the TR, KF, LC, and FC. The VFA is a foothold selection algorithm that continuously adapts the robot's trajectory based on the FEC. The VFA algorithm of this work extends our previous work in [38] and [49] as well as the state of the art [37], [46]. Since the computation of the FEC is usually expensive, we rely on approximating these criteria with CNNs.

The robot's skills and the notion of success provided by the FEC allowed the VPA to generate body poses that maximize the chances of success in reaching safe footholds. This resulted in body poses that are aware of the terrain and aware of what the robot and its legs can do. For that reason, the VPA was able to generate body poses that give a better chance for the VFA to select safe footholds. As a result, because of ViTAL, HyQ and HyQReal were able to traverse multiple terrains with various forward velocities and different gaits without colliding or reaching workspace limits. The terrains included stairs, gaps, and rough terrains, and the commanded velocities varied from 0.2 to 0.75 m/s. The VPA outperformed other strategies for pose adaptation. We compared VPA with the TBR, which is another VPA strategy, and showed that indeed the VPA puts the robot in a pose that provides the feet with higher number of safe footholds. Because of this, the VPA made our robots succeed in various scenarios where the TBR failed.

VIII. LIMITATIONS AND FUTURE WORK

One issue that we faced during experiment was in tracking the motion of the robot, especially for HyQReal. We were using a WBC for motion tracking. We believe that the motion tracking and our strategy can be improved by using a MPC alongside the WBC. Similarly, instead of using a model-based controller (MPC or WBC), we hypothesize that an RL-based controller can also improve the robustness and reliability of the overall robot behavior.

As explained in Section V, one other key limitation was regarding the perception system. State estimation introduced a significant drift that caused a major noise and drift in the terrain map. Albeit not being a limitation to the suggested approach, we plan on improving the state estimation and perception system of HyQ and HyQReal to allow us to test ViTAL in the wild.

The pose optimization problem of the VPA does not reason about the robot's dynamics. This did not prevent HyQ and HyQReal from achieving dynamic locomotion while traversing challenging terrains at high speeds. However, we believe that incorporating the robot's dynamics into ViTAL may result in a better overall performance. That said, we believe

that in the future, the VPA should also reason about the robot's dynamics. For instance, one can augment the FEC with another criterion that ensures that the selected footholds are dynamically feasible by the robot.

In addition, in the future, we plan to extend the VPA of ViTAL to not only send pose references, but also reason about the robot's body twist. We also plan to augment the robot skills to not only consider FEC, but also skills that are tailored to the robot pose. Finally, in this article, ViTAL considered heightmaps that are 2.5-D maps. In the future, we plan to consider full 3-D maps that will enable ViTAL to reason about navigating in confined space (inspired by [39]).

APPENDIX A CNN APPROXIMATION IN THE VFA AND THE VPA

In the VFA, the foothold evaluation stage is approximated with a CNN [65], as explained in Remark 3. The CNN approximates the mapping between T_{vfa} and p_* . The heightmap H_{vfa} in T_{vfa} passes through three convolutional layers with 5×5 kernels, 2×2 padding, leaky rectified linear unit (Leaky ReLU) activation [66], and 2×2 max-pooling operation. The resulted one-dimensional feature vector is concatenated with the rest of the variables in the tuple T_{vfa} , namely, z_h , v_b , α , and p_n . This new vector passes through two fully connected layers with Leaky ReLU and softmax activations. The parameters of the CNN are optimized to minimize the cross-entropy loss [67] of classifying a candidate foothold location as optimal p_* .

In the VPA, the pose evaluation and the function approximation are approximated with a CNN, as explained in Remark 5. The CNN infers the weights w of $\hat{\mathcal{F}}$ given T_{vpa} (the mapping between T_{vpa} and w). The heightmap $H_{\text{vpa}} \in \mathbb{R}^{33 \times 33}$ passes through three convolutional layers with 5×5 kernels, 2×2 padding, Leaky ReLU activation, and 2×2 max-pooling operation. The body velocities v_b pass through a fully connected layer with Leaky ReLU activation that is then concatenated with the one-dimensional feature vector obtained from the heightmap. This new vector passes through two fully connected layers with Leaky ReLU and linear activations. The parameters of this CNN are optimized to minimize the mean squared error loss between the number of safe footholds n_{sf} predicted by $\hat{\mathcal{F}}(z_h, w)$ and $\hat{\mathcal{F}}(z_h, \hat{w})$, where \hat{w} are the function parameters approximated by the CNN.

For both the CNNs, we used the Adam optimizer [68] with a learning rate of 0.001, and we used a validation-based early stopping using a 9-to-1 proportion to reduce overfitting. The datasets required for training this CNNs are collected by running simulated terrain scenarios that consist of bars, gaps, stairs, and rocks. In this article, we considered a 33×33 heightmap with a resolution of 0.02 m ($H_{\text{vfa}}, H_{\text{vpa}} \in \mathbb{R}^{33 \times 33}$).

APPENDIX B DETAILS ON THE FUNCTION APPROXIMATION OF THE VPA

As explained in Section IV-D, the function $\hat{\mathcal{F}}(z_h, w)$

$$\hat{\mathcal{F}}(z_h, w) = \sum_{e=1}^E w_e \cdot g(z_h, \Sigma_e, c_e) \quad (28)$$

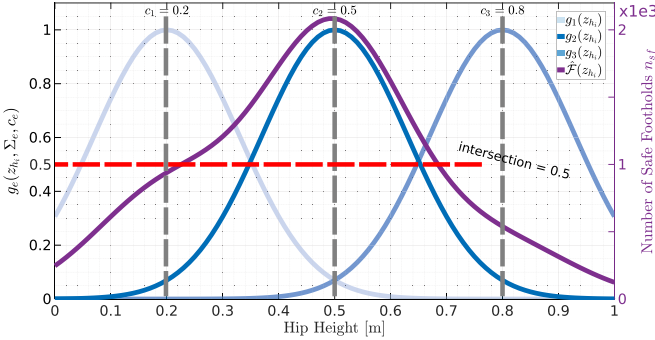


Fig. 15. Illustration of the function approximation of the VPA.

is defined as the weighted sum of Gaussian basis functions

$$g(z_{hi}, \Sigma_e, c_e) = \exp(-0.5(z_{hi} - c_e)^T \Sigma_e^{-1} (z_{hi} - c_e)). \quad (29)$$

The parameters Σ_e and c_e are the widths and centers of the Gaussian function g_e (see [57, Sec. 3.1]). In the literature, c_e is usually referred to as the mean or the expected value, and Σ_e as the standard deviation. The regression algorithm should predict the weights w_e and the parameters Σ_e and c_e . To reduce the dimensionality of the problem, as explained in Section IV-D, and in [57, Sec. 4.1], we decided to fix the values of the parameters of the Gaussian functions Σ_e and c_e . In detail, the centers c_e are spaced equidistantly within the bounds of the hip heights z_{hi} , and the widths are determined by the value at which the Gaussian functions intersect. That way, the regression algorithm only outputs the weights w_e . Fig. 15 shows an example of the function approximation. In this example, the bounds of the hip heights z_{hi} are 0.2 and 0.8 m. Assuming a number of basis functions $E = 3$, the centers c_e are then chosen to be equidistant within the bounds, and thus, the centers c_e are 0.2, 0.3, and 0.8 m. By choosing the Gaussian functions to intersect at 0.5, the widths Σ_e are 0.13.

APPENDIX C

REPRESENTING THE HIP HEIGHTS IN TERMS OF THE BODY POSE

To represent the hip heights in terms of the body pose, we first write the forward kinematics of the robot's hips

$$p_{hi}^W = p_b^W + R_b^W p_{hi}^b \quad (30)$$

where $p_{hi}^W \in \mathbb{R}^3$ is the position of the hip of the i th leg in the world frame, $p_b^W \in \mathbb{R}^3$ is the position of the robot's base in the world frame, $R_b^W \in SO(3)$ is the rotation matrix mapping vectors from the base frame to the world frame, and $p_{hi}^b \in \mathbb{R}^3$ is the position of the hip of the i th leg in the base frame. The rotation matrix R_b^W is a representation of the Euler angles of the robot's base with sequence of roll β , pitch γ , and yaw ψ (Cardan angles) [69]. The variable p_{hi}^b is obtained from the computer-aided design of the robot. Expanding (30) yields

$$\begin{bmatrix} x_{hi}^W \\ y_{hi}^W \\ z_{hi}^W \end{bmatrix} = \begin{bmatrix} x_b^W \\ y_b^W \\ z_b^W \end{bmatrix} + R_b^w(\beta, \gamma, \psi) \begin{bmatrix} x_{hi}^b \\ y_{hi}^b \\ z_{hi}^b \end{bmatrix} \quad (31)$$

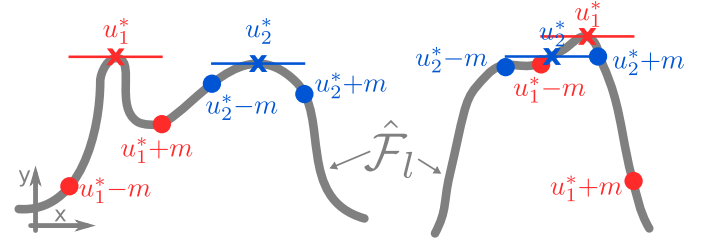


Fig. 16. Using the sum of squared integrals as a cost function in the pose optimization of the VPA. The two curves represent $\hat{\mathcal{F}}_l$. The x -axis is the hip height and the y -axis is n_{sf} . The figure shows two optimal poses: u_1^* that is from using \mathcal{C}_{sum} or $\mathcal{C}_{\text{prod}}$, and u_2^* that is from using \mathcal{C}_{int} .

$$= \begin{bmatrix} x_b^W \\ y_b^W \\ z_b^W \end{bmatrix} + \begin{bmatrix} \dots & \dots & \dots \\ \dots & \dots & \dots \\ -s\gamma & c\gamma s\beta & c\gamma c\beta \end{bmatrix} \begin{bmatrix} x_{hi}^b \\ y_{hi}^b \\ z_{hi}^b \end{bmatrix} \quad (32)$$

where s and c are sine and cosine of the angles, respectively. Since we are interested only in the hip heights, the z -component (third row) of (32) yields

$$z_{hi}^W = z_b^W - x_{hi}^b s\gamma + y_{hi}^b c\gamma s\beta + z_{hi}^b c\gamma c\beta. \quad (33)$$

APPENDIX D

DETAILS ON USING THE SUM OF SQUARED INTEGRALS AS A COST FUNCTION IN THE POSE OPTIMIZATION PROBLEM OF THE VPA

Using \mathcal{C}_{int} as a cost function can be motivated by taking Fig. 16 as an example. In this figure, there are two curves that represent $\hat{\mathcal{F}}_l$, where the horizontal axis is the hip height and the vertical axis represent n_{sf} . The figure shows two optimal poses where u_1^* is the optimal pose using the cost functions \mathcal{C}_{sum} or $\mathcal{C}_{\text{prod}}$ that only maximize for $\hat{\mathcal{F}}_l$, and u_2^* is the optimal pose using the cost function \mathcal{C}_{int} . As shown in the figure, if \mathcal{C}_{sum} or $\mathcal{C}_{\text{prod}}$ is used, the optimal pose will be u_1^* , which is indeed the one that results in the maximum $\hat{\mathcal{F}}_l$. However, if there is a tracking error of m (thus the robot reaches $u_1^* \pm m$), the robot might end up in the pose $u_1^* \pm m$ that results in a small number of safe footholds. Using \mathcal{C}_{int} will take into account the safe footholds within a margin m . This might result in a pose that does not yield the maximum number of safe footholds, but it will result in a safer foothold in case the robot pose has any tracking errors. Note that using the sum of squared integrals \mathcal{C}_{int} as a cost function is similar to smoothing $\hat{\mathcal{F}}_l$ with respect to the hip height (a moving average smoothing). Using a smoothing function \mathcal{C}_s may take the form

$$\mathcal{C}_s = \sum_{l=1}^{N_l=4} \left\| \frac{1}{2\epsilon} \sum_{i=-\epsilon}^{\epsilon} \hat{\mathcal{F}}_l(z_{hi} + i) \right\|_Q^2. \quad (34)$$

APPENDIX E

DEFINING THE RECEDING HORIZON

In the receding horizon, there is a tuple $T_{\text{vpa},j}$ for every j th horizon that is defined as

$$T_{\text{vpa},j} = (H_{\text{vpa},j}, v_b, \alpha) \quad (35)$$

hence sharing the same body twist v_b and gait parameters α but a different heightmap $H_{vpa,j}$. For every leg, a heightmap of horizon $j + 1$ is overlapping with the previous horizon's j heightmap. This overlap has a magnitude of Δh taking the same direction as the body velocity \dot{x}_b . Without loss of generality, we chose the magnitude of the overlap to be half of the diagonal size of the heightmap in this work. To sum up, we first gather $T_{vpa,j}$ that share the same v_b and α , but a different $H_{vpa,j}$. Then, we evaluate $T_{vpa,j}$ and approximate the output using the function approximation yielding $\hat{\mathcal{F}}_j$ that is sent to the optimizer for all of the legs.

APPENDIX F MISCELLANEOUS SETTINGS

In this article, all the simulations were conducted on an Intel Core i7 quad-core CPU, and all experiments were running on an onboard Intel Core i7 quad-core CPU where state estimation, mapping, and controls were running. The RCF (including the WBC) runs at 250 Hz, the low-level controller runs at 1000 Hz, the state estimator runs at 333 Hz, and the mapping algorithm runs at 20 Hz. The VPA and the VFA run asynchronously at the maximum possible update rate.

ViTAL is implemented in Python. The CNNs are implemented in PyTorch [70]. As explained in Appendix A, in this article, we considered a 33×33 heightmap with a resolution of 0.02 m ($H_{vfa}, H_{vpa} \in \mathbb{R}^{33 \times 33}$). The finite set $\bar{\mathcal{Z}}$ consisted of a hip height range between 0.2 and 0.8 m with a resolution of 0.02 m yielding $N_{z_h} = 31$ samples. The number of radial basis functions used in the function approximation was $E = 30$. The pose optimization problem is solved with a trust-region interior point method [71], [72], which is a nonlinear optimization problem solver that we solved using SciPy [73]. The bounds of the pose optimization problem u_{\min} and u_{\max} are $[0.2 \text{ m}, -0.35 \text{ rad}, -0.35 \text{ rad}]$, and $[0.8 \text{ m}, 0.35 \text{ rad}, 0.35 \text{ rad}]$, respectively. We used a receding horizon of $N_h = 2$ with a map overlap of half the size of the heightmap. For a heightmap of a size of 33×33 and a resolution of 0.02 m, the map overlap Δh is 0.33 m. We used Gazebo [74] for the simulations and ROS for communication.

APPENDIX G ESTIMATION ACCURACY

We compare the estimation accuracy of the VFA by comparing the output of the foothold evaluation stage (explained in Section III) given the same input tuple T_{vfa} . That is to say, we compare the estimation accuracy of the VFA by comparing $\hat{g}(T_{vfa})$ versus $g(T_{vfa})$ (see Remark 3). To do so, once trained, we generated a dataset of 4401 samples from randomly sampled heightmaps for every leg. This analysis was done on HyQ. As explained in Section III, from all of the safe candidate footholds in μ_{safe} , the VFA chooses the optimal foothold to be the one closest to the nominal foothold. Thus, to fairly analyze the estimation accuracy of the VFA, we present three main measures: *perfect match* being the amount of samples where $\hat{g}(T_{vfa})$ outputted the exact value of $g(T_{vfa})$, *safe footholds*, being the amount of samples where $\hat{g}(T_{vfa})$ did not output the exact

value of $g(T_{vfa})$, but rather a foothold that is safe but not closest to the nominal foothold, and *mean distance*, being the average distance of the estimated optimal foothold from $\hat{g}(T_{vfa})$ relative to the exact foothold from $g(T_{vfa})$. These measures are presented as the mean of all legs. Based on that, the perfect match measure is 74.0%. Thus, 74% of $\hat{g}(T_{vfa})$ perfectly matched $g(T_{vfa})$. The safe footholds measure is 93.7%. Thus, 93.7% of $\hat{g}(T_{vfa})$ were deemed safe. Finally, the mean distance of the estimated optimal foothold from $\hat{g}(T_{vfa})$ relative to the exact foothold from $g(T_{vfa})$ is 0.02 m. This means that, on average, $\hat{g}(T_{vfa})$ yielded optimal footholds that are 0.02 m far from the optimal foothold from $g(T_{vfa})$. Note that the radius of HyQ's foot and the resolution of the heightmap are 0.02 m, which means that the average distance measure is still acceptable especially since we account for this value in the uncertainty margin, as explained in Remark 1.

Similar to the VFA, we compare the accuracy of VPA by comparing the output of the pose evaluation stage (explained in Section IV-C) given the same input tuple T_{vfa} . That is to say, we compare the estimation accuracy of the VPA by comparing $\bar{\mathcal{F}}$ versus $\hat{\mathcal{F}}$ (see Remarks 4 and 5). To do so, we ran one simulation using the stairs setup shown in Fig. 5 on HyQ and gathered the input tuple T_{vfa} . Then, we ran the VPA offline, once with the exact evaluation (yielding $\bar{\mathcal{F}}$) and once with the approximate one (yielding $\hat{\mathcal{F}}$).

Based on this simulation run, the mean values of the exact and the approximate evaluations are $\text{mean}(\bar{\mathcal{F}}) = 1370$ and $\text{mean}(\hat{\mathcal{F}}) = 1322$, respectively. This yields an estimation accuracy $\text{mean}(\hat{\mathcal{F}})/\text{mean}(\bar{\mathcal{F}})$ of 96.5%.

APPENDIX H COMPUTATIONAL ANALYSIS

To analyze the computational time of the VFA and the VPA, we ran one simulation using the stairs setup shown in Fig. 5 on HyQ to gather the input tuples of the VFA and the VPA, T_{vfa} and T_{vpa} , respectively. Then, we ran both the algorithms offline, once with the exact evaluation and once using the CNNs, and collected the time it took to run both the algorithms (all stages included). The mean and standard deviation of the time taken to compute the exact and the CNN-approximated VFA (per leg) algorithms are $7.5 \text{ ms} \pm 1 \text{ ms}$, and $3.5 \text{ ms} \pm 1 \text{ ms}$, respectively. The mean and standard deviation of the time taken to compute the exact and the CNN-approximated VPA algorithms are $720 \text{ ms} \pm 68 \text{ ms}$, and $180 \text{ ms} \pm 60 \text{ ms}$, respectively. Hence, the VFA and the VPA can run at roughly 280 and 5 Hz, respectively. This also shows that the CNNs can speed up the evaluation of the VFA and the VPA up to four times and two times, respectively.

Note that it takes longer to compute the VFA of this work versus our previous work [38]. This is because the VFA of this work considers more inputs than in our previous work, and thus, the size of the CNN is larger. As can be seen, the VPA runs at a relatively lower update rate compared to the VFA. We believe that this is not an issue since the VFA runs at the legs level, while the VPA runs at the body level, which means that the legs experience faster dynamics than the body.

During simulations and experiments, the CNNs were running on a CPU. A significant amount of computational time can be

reduced if we run the CNNs of the VFA and the VPA on a GPU. Likewise, a significant amount of computational time can be reduced if a different pose optimization solver is used. However, both the suggestions are beyond the scope of this article and are left as a future work.

ACKNOWLEDGMENT

The authors would like to thank Geoff Fink and Chundri Boelens for the help provided in this article.

REFERENCES

- [1] J. Lee, J. Hwangbo, L. Wellhausen, V. Koltun, and M. Hutter, "Learning quadrupedal locomotion over challenging terrain," *Sci. Robot.*, vol. 5, no. 47, Oct. 2021, Art. no. eabc5986, doi: [10.1126/scirobotics.abc5986](https://doi.org/10.1126/scirobotics.abc5986).
- [2] C. Yang, K. Yuan, Q. Zhu, W. Yu, and Z. Li, "Multi-expert learning of adaptive legged locomotion," *Sci. Robot.*, vol. 5, no. 49, Dec. 2020, Art. no. eabb2174, doi: [10.1126/scirobotics.eabb2174](https://doi.org/10.1126/scirobotics.eabb2174).
- [3] C. Semini et al., "Brief introduction to the quadruped robot HyQReal," in *Proc. Italian Conf. Robot. Intell. Mach.*, Rome, Italy, 2019, pp. 1–2.
- [4] B. Katz, J. D. Carlo, and S. Kim, "Mini Cheetah: A platform for pushing the limits of dynamic quadruped control," in *Proc. IEEE Int. Conf. Robot. Autom.*, Montreal, QC, Canada, 2019, pp. 6295–6301, doi: [10.1109/ICRA.2019.8793865](https://doi.org/10.1109/ICRA.2019.8793865).
- [5] G. Bledt, M. J. Powell, B. Katz, J. Di Carlo, P. M. Wensing, and S. Kim, "MIT Cheetah 3: Design and control of a robust, dynamic quadruped robot," in *Proc. IEEE/RSJ Int. Conf. Intell. Robot. Syst.*, Madrid, Spain, 2018, pp. 2245–2252, doi: [10.1109/IROS.2018.8593885](https://doi.org/10.1109/IROS.2018.8593885).
- [6] M. Hutter et al., "Anymal—A highly mobile and dynamic quadrupedal robot," in *Proc. IEEE/RSJ Int. Conf. Intell. Robot. Syst.*, Daejeon, South Korea, 2016, pp. 38–44, doi: [10.1109/IROS.2016.7758092](https://doi.org/10.1109/IROS.2016.7758092).
- [7] *Spot*, Boston Dynamics, Waltham, MA, USA, 2021. Accessed: Aug. 2022. [Online]. Available: <https://www.bostondynamics.com/spot>
- [8] *Robots*, Agility Robotics, Albany, OR, USA, 2021. Accessed: Aug. 2022. [Online]. Available: <https://www.agilityrobotics.com/robots>
- [9] *Go1*, Unitree Robotics, Hangzhou, China, 2021. Accessed: Aug. 2022. [Online]. Available: <https://www.unitree.com/products/go1>
- [10] S. Fahmi, "On terrain-aware locomotion for legged robots," Ph.D. dissertation, Istituto Italiano di Tecnologia, Genoa, Italy, 2021.
- [11] R. Buchanan, J. Bednarek, M. Camurri, M. Nowicki, K. Walas, and M. Fallon, "Navigating by touch: Haptic Monte Carlo localization via geometric sensing and terrain classification," *Auton. Robot.*, vol. 45, pp. 843–857, Aug. 2021, doi: [10.1007/s10514-021-10013-w](https://doi.org/10.1007/s10514-021-10013-w).
- [12] S. Fahmi, G. Fink, and C. Semini, "On state estimation for legged locomotion over soft terrain," *IEEE Sens. Lett.*, vol. 5, no. 1, Jan. 2021, Art. no. 6000104.
- [13] S. Wang, A. Bhatia, M. T. Mason, and A. M. Johnson, "Contact localization using velocity constraints," in *Proc. IEEE/RSJ Int. Conf. Intell. Robot. Syst.*, Las Vegas, NV, USA, 2020, pp. 7351–7358.
- [14] A. Ahmadi, T. Nygaard, N. Kottege, D. Howard, and N. Hudson, "Semi-supervised gated recurrent neural networks for robotic terrain classification," *IEEE Robot. Autom. Lett.*, vol. 6, no. 2, pp. 1848–1855, Apr. 2021, doi: [10.1109/LRA.2021.3060437](https://doi.org/10.1109/LRA.2021.3060437).
- [15] H. C. Lin and M. Mistry, "Contact surface estimation via haptic perception," in *Proc. IEEE Int. Conf. Robot. Autom.*, Paris, France, 2020, pp. 5087–5093, doi: [10.1109/ICRA40945.2020.9196816](https://doi.org/10.1109/ICRA40945.2020.9196816).
- [16] S. Fahmi, M. Focchi, A. Radulescu, G. Fink, V. Barasuol, and C. Semini, "STANCE: Locomotion adaptation over soft terrain," *IEEE Trans. Robot.*, vol. 36, no. 2, pp. 443–457, Apr. 2020, doi: [10.1109/TRO.2019.2954670](https://doi.org/10.1109/TRO.2019.2954670).
- [17] K. Paigwar et al., "Robust quadrupedal locomotion on sloped terrains: A linear policy approach," in *Proc. Conf. Robot Learn.*, 2020, pp. 1–11.
- [18] L. Wellhausen, A. Dosovitskiy, R. Ranftl, K. Walas, C. Cadena, and M. Hutter, "Where should I walk? Predicting terrain properties from images via self-supervised learning," *IEEE Robot. Autom. Lett.*, vol. 4, no. 2, pp. 1509–1516, Jan. 2019, doi: [10.1109/LRA.2019.2895390](https://doi.org/10.1109/LRA.2019.2895390).
- [19] W. Bosworth, J. Whitney, S. Kim, and N. Hogan, "Robot locomotion on hard and soft ground: Measuring stability and ground properties in-situ," in *Proc. IEEE Int. Conf. Robot. Autom.*, Stockholm, Sweden, 2016, pp. 3582–3589, doi: [10.1109/ICRA.2016.7487541](https://doi.org/10.1109/ICRA.2016.7487541).
- [20] D. D. Fan, K. Otsu, Y. Kubo, A. Dixit, J. Burdick, and A. Aghamohammadi, "STEP: Stochastic traversability evaluation and planning for risk-aware off-road navigation," in *Proc. Robot.: Sci. Syst. Conf.*, 2021, pp. 1–12, doi: [10.15607/RSS.2021.XVII.021](https://doi.org/10.15607/RSS.2021.XVII.021).
- [21] O. Melon, R. Orsolino, D. Surovik, M. Geisert, I. Havoutis, and M. Fallon, "Receding-horizon perceptive trajectory optimization for dynamic legged locomotion with learned initialization," in *Proc. IEEE Int. Conf. Robot. Autom.*, Xi'an, China, 2021, pp. 9805–9811, doi: [10.1109/ICRA48506.2021.9560794](https://doi.org/10.1109/ICRA48506.2021.9560794).
- [22] B. Ponton, M. Khadiv, A. Meduri, and L. Righetti, "Efficient multicontact pattern generation with sequential convex approximations of the centroidal dynamics," *IEEE Trans. Robot.*, vol. 37, no. 5, pp. 1661–1679, Feb. 2021, doi: [10.1109/TRO.2020.3048125](https://doi.org/10.1109/TRO.2020.3048125).
- [23] C. Mastalli et al., "Crocoddyl: An efficient and versatile framework for multi-contact optimal control," in *Proc. IEEE Int. Conf. Robot. Autom.*, 2020, pp. 2536–2542, doi: [10.1109/ICRA40945.2020.9196673](https://doi.org/10.1109/ICRA40945.2020.9196673).
- [24] A. W. Winkler, C. D. Bellicoso, M. Hutter, and J. Buchli, "Gait and trajectory optimization for legged systems through phase-based end-effector parameterization," *IEEE Robot. Autom. Lett.*, vol. 3, no. 3, pp. 1560–1567, Jul. 2018, doi: [10.1109/LRA.2018.2798285](https://doi.org/10.1109/LRA.2018.2798285).
- [25] C. Mastalli, I. Havoutis, M. Focchi, D. G. Caldwell, and C. Semini, "Motion planning for quadrupedal locomotion: Coupled planning, terrain mapping and whole-body control," *IEEE Trans. Robot.*, vol. 36, no. 6, pp. 1635–1648, Dec. 2020, doi: [10.1109/TRO.2020.3003464](https://doi.org/10.1109/TRO.2020.3003464).
- [26] M. Brunner, B. Brüggemann, and D. Schulz, "Hierarchical rough terrain motion planning using an optimal sampling-based method," in *Proc. IEEE Int. Conf. Robot. Autom.*, Karlsruhe, Germany, 2013, pp. 5539–5544, doi: [10.1109/ICRA.2013.6631372](https://doi.org/10.1109/ICRA.2013.6631372).
- [27] H. Li and P. M. Wensing, "Hybrid systems differential dynamic programming for whole-body motion planning of legged robots," *IEEE Robot. Autom. Lett.*, vol. 5, no. 4, pp. 5448–5455, Oct. 2020, doi: [10.1109/LRA.2020.3007475](https://doi.org/10.1109/LRA.2020.3007475).
- [28] H. Li, R. J. Frei, and P. M. Wensing, "Model hierarchy predictive control of robotic systems," *IEEE Robot. Autom. Lett.*, vol. 6, no. 2, pp. 3373–3380, Apr. 2021, doi: [10.1109/LRA.2021.3061322](https://doi.org/10.1109/LRA.2021.3061322).
- [29] N. Rudin, D. Hoeller, P. Reist, and M. Hutter, "Learning to walk in minutes using massively parallel deep reinforcement learning," in *Proc. Conf. Robot Learn.*, London, U.K., 2021, pp. 91–100.
- [30] W. Yu et al., "Visual-locomotion: Learning to walk on complex terrains with vision," in *Proc. Conf. Robot Learn.*, London, U.K., 2021, pp. 1291–1302.
- [31] T. Miki, J. Lee, J. Hwangbo, L. Wellhausen, V. Koltun, and M. Hutter, "Learning robust perceptive locomotion for quadrupedal robots in the wild," *Sci. Robot.*, vol. 7, no. 62, Jan. 2022, Art. no. eabk2822, doi: [10.1126/scirobotics.abk2822](https://doi.org/10.1126/scirobotics.abk2822).
- [32] S. Gangapurwala, M. Geisert, R. Orsolino, M. Fallon, and I. Havoutis, "Real-time trajectory adaptation for quadrupedal locomotion using deep reinforcement learning," in *Proc. IEEE Int. Conf. Robot. Autom.*, Xi'an, China, 2021, pp. 1–7.
- [33] A. Kumar, Z. Fu, D. Pathak, and J. Malik, "RMA: Rapid motor adaptation for legged robots," in *Proc. Robot.: Sci. Syst. Conf.*, Jul. 2021, pp. 1–15, doi: [10.15607/RSS.2021.XVII.011Fe](https://doi.org/10.15607/RSS.2021.XVII.011Fe).
- [34] J. Siekmann, K. Green, J. Warila, A. Fern, and J. Hurst, "Blind bipedal stair traversal via sim-to-real reinforcement learning," in *Proc. Robot.: Sci. Syst. Conf.*, 2021, pp. 1–9, doi: [10.15607/RSS.2021.XVII.061](https://doi.org/10.15607/RSS.2021.XVII.061).
- [35] V. Tsounis, M. Alge, J. Lee, F. Farshidian, and M. Hutter, "DeepGait: Planning and control of quadrupedal gaits using deep reinforcement learning," *IEEE Robot. Autom. Lett.*, vol. 5, no. 2, pp. 3699–3706, Apr. 2020, doi: [10.1109/LRA.2020.2979660](https://doi.org/10.1109/LRA.2020.2979660).
- [36] M. Kalakrishnan, J. Buchli, P. Pastor, M. Mistry, and S. Schaal, "Learning, planning, and control for quadruped locomotion over challenging terrain," *Int. J. Robot. Res.*, vol. 30, no. 2, pp. 236–258, Nov. 2011, doi: [10.1177/0278364910388677](https://doi.org/10.1177/0278364910388677).
- [37] P. Fankhauser, M. Bjelonic, C. Dario Bellicoso, T. Miki, and M. Hutter, "Robust rough-terrain locomotion with a quadrupedal robot," in *Proc. IEEE Int. Conf. Robot. Autom.*, Brisbane, QLD, Australia, 2018, pp. 5761–5768, doi: [10.1109/ICRA.2018.8460731](https://doi.org/10.1109/ICRA.2018.8460731).
- [38] O. Villarreal et al., "Fast and continuous foothold adaptation for dynamic locomotion through CNNs," *IEEE Robot. Autom. Lett.*, vol. 4, no. 2, pp. 2140–2147, Apr. 2019, doi: [10.1109/LRA.2019.2899434](https://doi.org/10.1109/LRA.2019.2899434).
- [39] R. Buchanan, L. Wellhausen, M. Bjelonic, T. Bandyopadhyay, N. Kottege, and M. Hutter, "Perceptive whole-body planning for multilegged robots in confined spaces," *J. Field Robot.*, vol. 38, no. 1, pp. 68–84, Jun. 2021, doi: [10.1002/rob.21974](https://doi.org/10.1002/rob.21974).

- [40] P. Fernbach, S. Tonneau, and M. Taïx, "CROC: Convex resolution of centroidal dynamics trajectories to provide a feasibility criterion for the multi contact planning problem," in *Proc. IEEE/RSJ Int. Conf. Intell. Robot. Syst.*, Madrid, Spain, 2018, pp. 8367–8373, doi: [10.1109/IROS.2018.8593888](#).
- [41] S. Tonneau, A. Del Prete, J. Pettré, C. Park, D. Manocha, and N. Mansard, "An efficient acyclic contact planner for multiped robots," *IEEE Trans. Robot.*, vol. 34, no. 3, pp. 586–601, Jun. 2018, doi: [10.1109/TRO.2018.2819658](#).
- [42] J. Z. Kolter, M. P. Rodgers, and A. Y. Ng, "A control architecture for quadruped locomotion over rough terrain," in *Proc. IEEE Int. Conf. Robot. Autom.*, Pasadena, CA, USA, 2008, pp. 811–818, doi: [10.1109/ROBOT.2008.4543305](#).
- [43] M. Kalakrishnan, J. Buchli, P. Pastor, and S. Schaal, "Learning locomotion over rough terrain using terrain templates," in *Proc. IEEE/RSJ Int. Conf. Intell. Robot. Syst.*, St. Louis, MO, USA, 2009, pp. 167–172, doi: [10.1109/IROS.2009.5354701](#).
- [44] D. Belter and S. Piotr, "Rough terrain mapping and classification for foothold selection in a walking robot," *J. Field Robot.*, vol. 28, no. 4, pp. 497–528, Jun. 2011, doi: [10.1002/rob.20397](#).
- [45] V. Barasuol, M. Camurri, S. Bazeille, D. G. Caldwell, and C. Semini, "Reactive trotting with foot placement corrections through visual pattern classification," in *Proc. IEEE/RSJ Int. Conf. Intell. Robot. Syst.*, Hamburg, Germany, 2015, pp. 5734–5741, doi: [10.1109/IROS.2015.7354191](#).
- [46] F. Jenelten, T. Miki, A. E. Vijayan, M. Bjelonic, and M. Hutter, "Perceptual locomotion in rough terrain—Online foothold optimization," *IEEE Robot. Automat. Lett.*, vol. 5, no. 4, pp. 5370–5376, Oct. 2020, doi: [10.1109/LRA.2020.3007427](#).
- [47] D. Song et al., "Solving footstep planning as a feasibility problem using L1-norm minimization," *IEEE Robot. Autom. Lett.*, vol. 6, no. 3, pp. 5961–5968, Jul. 2021, doi: [10.1109/LRA.2021.3088797](#).
- [48] D. Belter, J. Bednarek, H. Lin, G. Xin, and M. Mistry, "Single-shot foothold selection and constraint evaluation for quadruped locomotion," in *Proc. IEEE Int. Conf. Robot. Autom.*, Montreal, QC, Canada, 2019, pp. 7441–7447, doi: [10.1109/ICRA.2019.8793801](#).
- [49] D. Esteban, O. Villarreal, S. Fahmi, C. Semini, and V. Barasuol, "On the influence of body velocity in foothold adaptation for dynamic legged locomotion via CNNs," in *Proc. Int. Conf. Climbing Walking Robot.*, Moscow, Russia, 2020, pp. 353–360, doi: [10.13180/clawar.2020.24-26.08.62](#).
- [50] D. Kim et al., "Vision aided dynamic exploration of unstructured terrain with a small-scale quadruped robot," in *Proc. IEEE Int. Conf. Robot. Autom.*, Paris, France, 2020, pp. 2464–2470, doi: [10.1109/ICRA40945.2020.9196777](#).
- [51] D. Belter and S. Piotr, "Posture optimization strategy for a statically stable robot traversing rough terrain," in *Proc. IEEE/RSJ Int. Conf. Intell. Robot. Syst.*, Vilamoura, Portugal, 2012, pp. 2204–2209, doi: [10.1109/IROS.2012.6385548](#).
- [52] D. Belter, "Efficient modeling and evaluation of constraints in path planning for multi-legged walking robots," *IEEE Access*, vol. 7, pp. 107845–107862, 2019, doi: [10.1109/ACCESS.2019.2933178](#).
- [53] O. Villarreal, V. Barasuol, P. M. Wensing, D. G. Caldwell, and C. Semini, "MPC-based controller with terrain insight for dynamic legged locomotion," in *Proc. IEEE Int. Conf. Robot. Autom.*, Paris, France, 2020, pp. 2436–2442, doi: [10.1109/ICRA40945.2020.9197312](#).
- [54] R. Buchanan, M. Camurri, and M. Fallon, "Haptic sequential Monte Carlo localization for quadrupedal locomotion in vision-denied scenarios," in *Proc. IEEE/RSJ Int. Conf. Intell. Robot. Syst.*, Las Vegas, NV, USA, 2020, pp. 3657–3663.
- [55] K. Green, Y. Godse, J. Dao, R. L. Hatton, A. Fern, and J. Hurst, "Learning spring mass locomotion: Guiding policies with a reduced-order model," *IEEE Robot. Autom. Lett.*, vol. 6, no. 2, pp. 3926–3932, Apr. 2021, doi: [10.1109/LRA.2021.3066833](#).
- [56] V. Barasuol, J. Buchli, C. Semini, M. Frigerio, E. R. De Pieri, and D. G. Caldwell, "A reactive controller framework for quadrupedal locomotion on challenging terrain," in *Proc. IEEE Int. Conf. Robot. Autom.*, Karlsruhe, Germany, 2013, pp. 2554–2561, doi: [10.1109/ICRA.2013.6630926](#).
- [57] F. Stulp and O. Sigaud, "Many regression algorithms, one unified model: A review," *Neural Netw.*, vol. 69, pp. 60–79, Sep. 2015, doi: [10.1016/j.neunet.2015.05.005](#).
- [58] M. Focchi, V. Barasuol, I. Havoutis, J. Buchli, C. Semini, and D. Gladwell, "Local reflex generation for obstacle negotiation in quadrupedal locomotion," in *Proc. Int. Conf. Climbing Walking Robot.*, Sydney, Australia, 2013, pp. 443–450, doi: [10.1142/9789814525534_0056](#).
- [59] S. Fahmi, C. Mastalli, M. Focchi, and C. Semini, "Passive whole-body control for quadruped robots: Experimental validation over challenging terrain," *IEEE Robot. Autom. Lett.*, vol. 4, no. 3, pp. 2553–2560, Jul. 2019, doi: [10.1109/LRA.2019.2908502](#).
- [60] T. Boaventura, J. Buchli, C. Semini, and D. Caldwell, "Model-based hydraulic impedance control for dynamic robots," *IEEE Trans. Robot.*, vol. 31, no. 6, pp. 1324–1336, Dec. 2015, doi: [10.1109/TRO.2015.2482061](#).
- [61] M. Camurri et al., "Probabilistic contact estimation and impact detection for state estimation of quadruped robots," *IEEE Robot. Autom. Lett.*, vol. 2, no. 2, pp. 1023–1030, Apr. 2017, doi: [10.1109/LRA.2017.2652491](#).
- [62] C. Semini, N. G. Tsagarakis, E. Guglielmino, M. Focchi, F. Cannella, and D. G. Caldwell, "Design of HyQ—A hydraulically and electrically actuated quadruped robot," *Proc. Inst. Mech. Eng. Part I. J. Syst. Control Eng.*, vol. 225, no. 6, pp. 831–849, 2011, doi: [10.1177/0959651811402275](#).
- [63] P. Fankhauser and M. Hutter, "A universal grid map library: Implementation and use case for rough terrain navigation," in *Robot Operating System (ROS): The Complete Reference*, vol. 1, A. Koubaa, Ed. Cham, Switzerland: Springer, Feb. 2016, pp. 99–120.
- [64] S. Fahmi, V. Barasuol, D. Esteban, O. Villarreal, and C. Semini, "ViTAL accompanying video," YouTube, Nov. 2021. Accessed: Aug. 2022. [Online]. Available: <https://youtu.be/b5Ea7Jf6hb0>
- [65] Y. Le Cun, B. Boser, J. S. Denker, D. Henderson, R. E. Howard, and L. D. J. W. Hubbard, "Handwritten digit recognition with a back-propagation network," in *Proc. Int. Conf. Neural Inf. Process.*, Cambridge, MA, USA, 1989, pp. 396–404.
- [66] A. L. Maas, A. Y. Hannun, and A. Y. Ng, "Rectifier non-linearities improve neural network acoustic models," in *Proc. Int. Conf. Mach. Learn.*, Atlanta, GA, USA, 2013, pp. 1–6.
- [67] C. M. Bishop, *Pattern Recognition and Machine Learning*, 1st ed. New York, NY, USA: Springer-Verlag, 2006.
- [68] D. P. Kingma and J. L. Ba, "Adam: A method for stochastic optimization," in *Proc. Int. Conf. Learn. Represent.*, San Diego, CA, USA, May 2015, pp. 1–15. [Online]. Available: <http://arxiv.org/abs/1412.6980>
- [69] J. Diebel, "Representing attitude: Euler angles, unit quaternions, and rotation vectors," Stanford Univ., Stanford, CA, USA, Tech. Rep., Oct. 2006. [Online]. Available: https://www.astro.rug.nl/software/kapteyn-beta/_downloads/attitude.pdf
- [70] A. Paszke et al., "PyTorch: An imperative style, high-performance deep learning library," in *Proc. Int. Conf. Neural Inf. Process. Syst.*, Vancouver, BC, Canada, 2019, pp. 8026–8037.
- [71] J. Nocedal and S. J. Wright, *Numerical Optimization*, vol. 17. New York, NY, USA: Springer, 1996.
- [72] R. H. Byrd, M. E. Hribar, and J. Nocedal, "An interior point algorithm for large-scale non-linear programming," *SIAM J. Optim.*, vol. 9, no. 4, pp. 877–900, Sep. 2021, doi: [10.1137/S1052623497325107](#).
- [73] P. Virtanen et al., "SciPy 1.0: Fundamental algorithms for scientific computing in Python," *Nature Methods*, vol. 17, no. 3, pp. 261–272, 2020.
- [74] N. Koenig and A. Howard, "Design and use paradigms for gazebo, an open-source multi-robot simulator," in *Proc. IEEE/RSJ Int. Conf. Intell. Robot. Syst.*, St. Louis, MO, USA, 2004, pp. 2149–2154, doi: [10.1109/IROS.2004.1389727](#).



Shamel Fahmi (Student Member, IEEE) was born in Cairo, Egypt. He received the B.Sc. degree in mechatronics from the German University in Cairo, Cairo, Egypt, in 2015, the M.Sc. degree in systems and control from the University of Twente, Enschede, The Netherlands, in 2017, and the Ph.D. degree in advanced and humanoid robotics from the Italian Institute of Technology, Genoa, Italy, in 2021.

His Ph.D. was focused on terrain-aware locomotion for legged robots. He is currently a Researcher with the Biomimetic Robotics Lab, Massachusetts

Institute of Technology, Cambridge, MA, USA. His research interests include locomotion planning and control for quadruped and humanoid robots using model- and learning-based methods.



Victor Barasoul received the Diploma in electrical engineering from the Universidade do Estado de Santa Catarina, Joinville, Brazil, in 2006, and the M.Sc. degree in electrical engineering and the Ph.D. degree in automation and systems engineering from the Universidade Federal de Santa Catarina, Florianópolis, Brazil, in 2008 and 2013, respectively.

He is currently a Researcher with the Dynamic Legged Systems Lab, Istituto Italiano di Tecnologia, Genoa, Italy. He is knowledgeable from the kinematic design to the control of hydraulic quadruped robots,

with major expertise in dynamic motion generation and control. His research interests include proprioceptive-based and exteroceptive-based reactions, whole-body control, machine learning for locomotion, active impedance modulation, and loco-manipulation.



Octavio Villarreal received the M.Sc. degree in mechanical engineering track control engineering from the Delft University of Technology, Delft, The Netherlands, in 2016, and the Ph.D. degree in vision-based foothold adaptation and locomotion strategies for legged robots from the Dynamic Legged Systems Lab, Istituto Italiano di Tecnologia, Genoa, Italy, and the University of Genoa, Genoa, in 2019.

He is currently a Robotics Research Engineer with Dyson Technology Ltd., Malmesbury, U.K.



Domingo Esteban received the B.Sc. degree in industrial engineering from the Universidad Nacional de San Agustín, Arequipa, Peru, in 2009, the M.Sc. degree in robotics and automation from the Universidad Carlos III, Madrid, Spain, in 2014, and the Ph.D. degree in advanced and humanoid robotics from the Italian Institute of Technology (IIT), Genoa, Italy, in 2019.

From 2019 to 2021, he was a Postdoctoral Researcher with the Dynamic Legged Systems Lab, IIT. He is currently with ANYbotics AG, Zurich, Switzerland. His research interests include machine learning for decision making and motion control in robotics.



Claudio Semini (Member, IEEE) received the M.Sc. degree in electrical engineering and information technology from ETH Zurich, Zurich, Switzerland, in 2005, and the Ph.D. degree in humanoid technologies from the Istituto Italiano di Tecnologia (IIT), Genoa, Italy, in 2010.

During his doctorate, he developed the hydraulic quadruped robot HyQ and worked on its control. Since 2012, he has been leading the Dynamic Legged Systems Lab, IIT. He is/was the coordinator/partner of several European Union, National, and Industrial projects (including HyQ-REAL, INAIL Teleop, Moog@IIT joint lab, ESA-ANT, etc.). His research interests include the design and control of highly dynamic and versatile legged robots for real-world operations, locomotion, and hydraulics.

Dr. Semini is a Co-Founder of the Technical Committee on Mechanisms and Design of the Robotics and Automation Society.